Evolution of Heat Flow, Hydrothermal Circulation and Permeability on the Young Southern Flank of the Costa Rica Rift

Kannikha Parameswari Kolandaivelu[1], Robert N. Harris[2], Robert P. Lowell[1], Adam H. Robinson[3], Dean J. Wilson[3], and Richard W. Hobbs[3]

[1]Department of Geosciences, Virginia Polytechnic Institute and State University, Blacksburg, VA 24061

kannikha@vt.edu (Corresponding author)

[2]College of Earth, Ocean, and Atmospheric Sciences, Oregon State University, Corvallis, OR 97331

[3]Department of Earth Sciences, Durham University, Durham DH1, United Kingdom

Key points:

1. Hydrothermal circulation accounts for 70% of the heat transfer from the southern flank of Costa Rica Rift (CRR) between ages of 1.6 to 5.7 Ma.

2. Advective heat loss is explained by combination of outcrop to outcrop circulation, discharge through faults, and heat loss through elevated basement topography.

3. Crustal permeability varies substantially as a function of age, and tends to correlate with seismic tomography data that suggest the spreading rate at the CRR varies with age as a result of episodic changes in magma supply and tectonic processes.

Abstract

We analyze 67 new conductive heat flow measurements on the southern flank of the Costa Rica Rift (CRR). Heat flow measurements cover five sites ranging in oceanic crustal age between approximately 1.6 and 5.7 Ma, and are co-located with a high-resolution multi-channel seismic line that extends from slightly north of the first heat flow site (1.6 Ma) to beyond ODP Hole 504B in 6.9 Ma crust. For the five heat flow sites, the mean observed conductive heat flow is ≈ 85 mWm^{-2}. This value is approximately 30% of the mean lithospheric heat flux expected from a half-space conductive cooling model, indicating that hydrothermal processes account for about 70% of the heat loss. The advective heat loss fraction varies from site to site and is explained by a combination of outcrop to outcrop circulation through exposed basement outcrops and discharge through faults. Super-critical convection in Layer 2A extrusives occurs between 1.6 and 3.5 Ma, and flow through a thinly-sedimented basement high occurs at 4.6 Ma. Advective heat loss diminishes rapidly between ≈ 4.5 and ≈ 5.7 Ma, which contrasts with plate cooling reference models that predict a significant deficit in conductive heat flow up to ages $\approx 65 \pm 10$ Ma. At ≈ 5.7 Ma the CRR topography is buried under sediment with an average thickness ≈ 150 m, and hydrothermal circulation in the basement becomes sub-critical or perhaps marginally critical. The absence of significant advective heat loss at ≈ 5.7 Ma at the CRR is thus a function of both burial of basement exposure under the sediment load and a reduction in basement permeability that possibly occurs as result of mineral precipitation and original permeability at the time of formation. Permeability is a non-monotonic function of age along the southern flank of the CRR, in general agreement with seismic velocity tomography interpretations that reflect variations in the degree of ridge-axis magma supply and tectonic extension. Hydrothermal circulation in the young oceanic crust at southern flank of CRR is affected by the interplay and complex interconnectedness of variations in permeability, sediment thickness, topographical structure, and tectonic and magmatic activities with age.

Key Words: heat flow, permeability and porosity, hydrothermal systems, hydrogeophysics

1. Introduction

The temporal and spatial evolution of oceanic crust and lithosphere are largely controlled by thermally mediated processes. Parsons & Sclater (1977), Stein & Stein (1994), Hasterok (2013) and Cheng (2016) have derived somewhat different plate cooling models based on global heat flow determinations and using various functions based on oceanic crustal age. The widely used Stein & Stein (1992) model was derived from a global analysis of heat flow and bathymetry data and suggests that predicted conductive heat flow from cooling lithosphere follows the expressions:

$$q_b = 510 \, \tau^{-1/2} \quad \text{for } 1 \text{ Ma} \leq \tau \leq 55 \text{ Ma} \tag{1a}$$

$$q_b = 48 + 96 \exp(-\tau/36) \quad \text{for } \tau > 55 \text{Ma} \tag{1b}$$

where q_b is the heat flow in mWm^{-2} and τ is the lithospheric age in Ma.

Measurements of conductive heat flow, particularly in young crust, typically lie well below conductive cooling curves (Baker *et al.* 1991; Langseth *et al.* 1992; Fisher *et al.* 2003a; Hutnak *et al.* 2008). This discrepancy has long been attributed to heat loss by hydrothermal circulation (e.g., Elder, 1965; Langseth & Von Herzen, 1970; Lister, 1972) and on a global scale, the difference between observed and predicted conductive heat loss indicates that hydrothermal circulation accounts for about 30% of the global oceanic heat flux (e.g., Williams & Von Herzen, 1974; Sclater *et al.* 1980; Elderfield & Schultz, 1996; Davies & Davies, 2010; Hasterok, 2013). Of this, approximately 20% to 30% occurs between 0 and 1 Ma, with the remainder occurring off axis (Stein & Stein, 1994; Elderfield & Schultz, 1996). Figure 1a shows the predicted cooling curve from equations (1a, 1b) along with globally observed values with their standard deviation averaged in 2 Ma bins.

The style of hydrothermal circulation and heat transfer changes as the crust and lithosphere age from "active" high-temperature magma-driven hydrothermal circulation at ages <0.1 Ma (Macdonald, 1982) to "passive" lower temperature circulation on the ridge flanks (Lister, 1982). The style of ridge flank hydrothermal circulation also evolves with lithospheric age. Passive circulation may initially extend to a depth of 6 km into the young crust (Cherkaoui *et al.* 2003; Craft & Lowell, 2009; Theissen-Krah *et al.* 2011; Hasenclever *et al.* 2014), and this deep crustal cooling may affect thermal regime of the ridge flank to an age of ~ 5 Ma (Spinelli & Harris, 2011). As the lithosphere ages the circulation tends to be restricted to the extrusive layer (Fisher, 1998; Becker & Davis, 2004), which typically consists of a highly permeable layer ≈ 150 m thick overlying a less permeable extrusive layer ≈ 400 m thick (Becker, 1985; Salisbury *et al.* 1985). The extrusive layer, commonly referred to as crustal Layer 2A, will be designated as 2A*u* and 2A*l* to represent the upper and lower extrusive layers, respectively. As sediment thickness increases, recharge and discharge becomes restricted to exposed basement and faults (Wheat *et al.* 2004; Hutnak *et al.* 2006; 2008; Fisher & Harris, 2010; Anderson *et al.* 2012).

As the thickness of low permeability sediments increases and oceanic basement topography becomes fully covered, fluid discharge to the ocean declines. Moreover, mineral precipitation and alteration may reduce crustal permeability, and reduced buoyancy forces may also impact the vigor of hydrothermal circulation (e.g., Jarrard *et al.* 2003). The conductive heat flow gradually approaches the predicted lithospheric cooling curve due to these processes that decrease the driving forces and increase impeding forces for hydrothermal circulation.

When the conductive heat flow and the cooling curve coincide, the crust is termed "sealed" (e.g., Anderson & Hobart, 1976; Stein & Stein, 1994), implying that hydrothermal circulation no longer affects the surface heat flow significantly. A statistical analysis of the global heat flow data set indicates that on average the sealing age corresponds to a basement age of 65±10 Ma (Figure 1a)

(Stein & Stein, 1994). This condition does not mean that hydrothermal circulation is absent. Rather it indicates that if hydrothermal circulation is present it is simply redistributing heat within the crust and does not transfer heat by advection from the crust to the ocean. Studies show that significant advective fluid flow can occur at basement ages much older than the global average "sealing age" (e.g., Embley *et al.* 1983; Von Herzen, 2004; Fisher & Von Herzen, 2005).

The dominant mechanism leading to the cessation of advective heat loss through the seafloor is debated. Based on their analysis of the global data set, Stein & Stein (1994) argue that hydrothermal flow decreases as a result of decreased layer 2 porosity and permeability rather than from burial by sediment. This argument runs counter to results from heavily sedimented ridges. Detailed heat flow studies on the thickly sedimented eastern flank of the Juan de Fuca Ridge (JDFR) (Davis *et al.* 1997; 1999; Fisher *et al.* 2003b; Spinelli & Fisher, 2004) show that mean observed heat flow reaches the predicted curve at ∼ 1.5 Ma. In addition, heat flow studies at the Costa Rica Rift (CRR) flank showed that the mean heat flow was near the predicted cooling curve near ODP Hole 504B, for which the crustal age was initially estimated to be 5.9 Ma (Hobart *et al.* 1985; Langseth *et al.* 1983, 1988, Davis *et al.* 2004). Revised estimates based on magnetics data suggest the crustal age at Hole 504B is ≈ 6.9 Ma (Wilson & Hey, 1995; Worm *et. al.* 1996; Wilson *et al.* 2003) which we adopt in this paper. Although ≈ 6.9 Ma is older than the previously estimated ≈ 5.9 Ma for Hole 504B, the conductive cooling curve is relatively flat over this 1 Ma age difference. The studies on heavily sedimented ridges suggest that the accumulation of relatively impermeable and laterally continuous sediment is the likely cause of a sealed system at these locations. Further, global compilations of permeability measurements and seismic velocity indicates that the greatest change in the physical properties of the basement occurs in the first 10 Ma (Fisher & Becker, 2000), leaving the role of crustal permeability in the sealing age an open question.

Heat flow studies on the flanks of young heavily sedimented oceanic crust such as JDFR and CRR provide opportunities to better understand the evolution of hydrothermal circulation and mechanisms of advective heat transport within a limited age and distance from the spreading center. In addition, such studies provide insight into crustal alteration (e.g., Alt, 1995), seismic velocity structure (e.g., Carlson, 2011, 2014) and microbial processes (e.g., Huber *et al.* 2003) that are linked to the thermal regime of the crust.

In this paper, we analyze 67 new conductive heat flow measurements from the southern flank of the CRR at sites ranging in age between ~1.6 and ~ 5.7 Ma. In our analysis, we also include previously collected heat flow data (Anderson & Hobart, 1976; Langseth *et al.* 1983, 1988; Hobart *et al.* 1985; Davis *et al.* 2003, 2004). The new sites are labeled PB02 to PB06 (Figure 2) and are co-located along a seismic reflection and multibeam bathymetry profiles, which enable an integrated analysis that elucidates the influence of basement topography and sediment thickness on fluid flow, advective heat transport, and changes in the hydrothermal regime as the crust evolves with age.

2. Geologic Setting

The Panama Basin, located in the equatorial Pacific, is bounded by the Cocos Ridge to the north and west, Carnegie Ridge to the south, and Ecuador Trench and Americas to the east. Three spreading centers are located in the basin: Costa Rica Rift (CRR), Ecuador Rift (ER), and the Galapagos Rift (GR) (Lonsdale & Kiltgord, 1978) (Figure 2). The southern flank of the CRR, the focus of our study, has an average half-spreading rate of approximately 3.3 cm yr^{-1} based on the distance from the CRR axis to the Hole 504B of age 6.9 Ma (Wilson & Hey, 1995; Worm *et. al.* 1996; Wilson *et al.* 2003). The green box (Figure 2) shows the region where complementary geophysical measurements were made. The seismic reflection profile, the locations of heatflow and other geophysical data, including swath bathymetry are shown in Figure 2.

3. Data

3.1 Seismic Reflection Measurements

A 270 km high-resolution seismic reflection profile (RS-A), along which heat flow measurements were co-located, was collected with a GI airgun array with a source frequency ranging between 20 and 200 Hz recorded on a 4500 m multichannel hydrophone streamer with a 12.5 m group length. The resulting imaging of the sediment and upper oceanic crust provides a geologic framework for interpreting the heat flow data. The complete seismic section (Figure 3) shows that sediment thickness varies considerably with thin sediment accumulations at basement highs, and thicker sediment accumulations at basement lows; the mean sediment thickness increasing from approximately 40 m at 1.6 Ma crust to 275 m at Hole 504B. The seismic profile also shows exposed basement, through going faults, and rough basement topography; however, for crust older than 5.7 Ma ($\approx$ 190 km in Figure 3), the basement topography is more subdued and becomes completely covered with sediment.

3.2 Heat Flow Data

Conductive heat flow measurements were acquired in sediments between 50 m to 250 m thick by means of a "violin-bow" type multi-penetration heat flow probe (Hyndman *et.al.* 1979). It consists of a 3.5 m sensor tube that houses 11 thermistors and heater wire that is offset from a lance. The configuration allows the probe to be gravity-driven into the sediments and provides the sensitivity to make precise and accurate heat flow measurements while also being robust so that many measurements can be made by 'pogo-ing' the probe along the bottom. A weight stand containing the data logger and telemetry system sits above the thermistor tube. In addition to logging the temperature time series, the data logger also records tilt, pressure, time, and the bottom water temperature. An ultra-short baseline sensor attached 50 m above the probe provides precise navigation. The probe allows in-situ measurements of the shallow thermal gradients and thermal

conductivity in sediments on the seafloor. The analysis of heat flow measurements is based on the scheme presented by Villinger & Davis (1987) as implemented using SlugHeat (Stein & Fisher, 2001). The in-situ thermal gradient is based on a temperature-time series collected for seven minutes, which is long enough to achieve partial equilibrium with the sediments. Equilibrium temperatures are then estimated through an extrapolation based on a line source model of radial heat conduction (Villinger & Davis, 1987). A calibrated heat pulse is then applied through the heater wire for ten seconds and a seven minute temperature decay provides data for determining thermal conductivity. The heat flow, thermal conductivities, thermal gradient values and sediment thicknesses for all sites are given in Table 1. Heat flow measurements were closely spaced to avoid aliasing the hydrothermal circulation signal and co-located with the swath bathymetry and seismic reflection data to better understand the measuring environment (e.g., Fisher & Harris, 2010).

4. Analysis

Figure 1b shows the 67 new measured heat flow values along with the previously published data (Anderson & Hobart, 1976; Langseth *et al.* 1983, 1988; Hobart *et al.* 1985; Davis *et al.* 2003, 2004) and predicted heat flow based on half-space cooling curve from equation (1a). Figure 1b shows heat flow transitioning from values of about 40 mWm^{-2} at 1.6 Ma to a mean value of 235 mWm^{-2} at 5.7 Ma, which lies near the predicted cooling curve. Previously published heat flow data indicated by open circles in Figure 1b also show that heat transfer transitions from advectively to conductively dominated values between ≈ 4.5 and ≈ 6.0 Ma.

The average measured heat flow of the 67 new measurements (Table 1) is ~ 85 mWm^{-2}. This value is considerably less than the average expected basal heat flow of ~ 280 mWm^{-2}, obtained by integrating equation (1a) between 1.6 Ma and 5.7 Ma. The heat flow fraction (q_{obs}/q_b) is ~ 0.3

indicating that ~ 70% (~ 200 mWm[-2]) of q_b is advected. The effect of thermal rebound from deep axial cooling on the south flanks of the CRR's between 1.6 to 5.7 Ma crust is small based on observational constraints and modeling studies (Fisher, 2003; Spinelli & Harris, 2011). Hence these effects on the overall advective heat loss fraction are negligible.

In order to quantify the mechanisms responsible for this advective heat loss, we construct a one-dimensional thermal conduction model of the sediment and basement as a function of age between 1.6 and 6.9 Ma at Hole 504B. This model allows us to compare the expected temperature at the sediment-basement interface (SBI) with the SBI temperature derived from the observed heat flow measurements. The mathematical formulation is given in Appendix A. The results given by equation (A.2) show that the conduction-derived SBI temperature, expressed as the difference ΔT_{SBI} between seafloor and base of the sediment can be written as

$$\Delta T_{SBI}(h_s) = \frac{q_b h_s}{\lambda_s} = \frac{510\tau^{1/2}v_s}{\lambda_s} \tag{2}$$

where $510\,\tau^{-1/2}$ is heat flow in mWm[-2], h_s is the sediment thickness, λ_s is the thermal conductivity of the sediment, and v_s is the sedimentation rate. Over much of heat flow profile, the sedimentation rate is ≈ 25 mMa[-1] whereas at PB04 and PB06 it is ≈ 40mMa[-1], similar to that at Hole 504B (Becker et al., 1983). Definitions and values of symbols are given in Table 2. We use λ_s = 0.92 Wm[-1]K[-1] which is the average thermal conductivity based on Hole 504B's physical properties measurements (Davis *et. al.*, 2004). Figure 4 shows the expected SBI temperature versus age for the two sedimentation rates, along with the average SBI temperature for the 5 heat flow sites and the data at Hole 504B. The observed SBI temperature at each heat flow point is determined from the relationship $\Delta T_{SBI}^{obs} = \frac{q_{obs} h_s}{\lambda_s}$. The average SBI temperature at each site, except PB06 and Hole 504B, is much less than predicted by conduction regardless of the sedimentation rate (Figure 4).

In the extrusive layer of the young oceanic crust south of the CRR, super-critical thermal convection will tend to homogenize the temperature distribution within the basement rocks. The condition for onset of convection is defined by the Rayleigh number Ra. For a layer of thickness h_b, with a fixed heat flux q_b at the base, and impermeable sediments above (Spinelli *et al.* 2004), the Rayleigh number and its critical value Ra_c is given by (Nield, 1968).

$$Ra = \frac{\alpha g k q_b h_b^2}{\lambda_b a^* \nu} \geq Ra_c = 27.1 \tag{3}$$

Assuming other parameters are constant, equation (3) shows that Ra decreases as $\tau^{1/2}$ as the crust ages because of the predicted decline of q_b. Using parameter values in Table 2, Figure 5 displays the crustal permeability needed to exceed Ra_c for h_b = 150 m and h_b = 550 m as a function of age. These values of h_b are chosen based on logging data from Hole 504B that indicates the upper 100-200 m of the crust is significantly more permeable than then underlying extrusive section, which extends to approximately 550 m beneath the sediments (Becker *et al.* 1989). The curves in Figure 5 show that super-critical convection at 1.6 Ma requires that k must exceed a threshold value k_{th} = 3 x 10^{-12} m^2 and 2 x 10^{-13} m^2, for h_b = 150 and 550 m, respectively; whereas k_{th} must exceed 7 x 10^{-12} m^2 and 5 x 10^{-13} m^2 at 6.9 Ma for the same values of h_b. The permeability value for h_b = 550 m is an "effective" value for combined Layers 2A*u* and 2A*l*, but since the thickness of 2A*l* is considerably greater than that of 2A*u*, it is assumed that the effective permeability is nearly the same as that of Layer 2A*l*.

When $Ra \gg Ra_c$ in a permeable layer with a given basal heat flux, vigorous convection tends to homogenize the temperature within in the convecting interior, but because the heat flux is fixed, fluid convection will transport the same amount of heat as the conducting layer, hence the Nusselt number is unity. Heat advection within the basement interior will be transported across the SBI by conduction across a thin thermal boundary layer so that both heat flux and temperature at the SBI are continuous. Hence the high Ra super-critical convection regime would not by itself result in a

reduction in conductive heat flow across the sediment layer or a decrease in SBI temperature, unless fluid advection can occur through the sediment layer or some other process such as outcrop to outcrop circulation or fluid discharge through faults also takes place. The observation in Figure 4 that SBI temperature is much less than predicted from conduction at sites PB02 through PB05 indicates that advective heat transfer is occurring. At PB06, however, the mean SBI temperature is only slightly less than the value predicted by conduction, suggesting that heat is not being advected between the crustal aquifer and the ocean.

In the following subsections, we present a detailed analysis of the heat flow data as a function of age from the five heat flow sites labeled PB02 through PB06. This analysis provides estimates of crustal permeability that can be compared with the Rayleigh criterion shown in Figure 5. The goal is to determine whether there appear to be significant changes in crustal permeability as a function of age that affects the advective heat transfer. The values of calculated permeability are given in Table 3. In performing these analyses, we neglect the effects of heat flow refraction, fluid flow through the sediments, and the effect of sedimentation on reducing the observed heat flow (e.g., Hutchinson, 1985; Hutnak & Fisher, 2007).

Our estimates of mass flow rate and crustal permeability in the basement are largely based on the well-mixed aquifer model in which we assume flow is dominantly parallel to the spreading direction. In reality fluid flow is likely 3D (e.g., Winslow & Fisher, 2015; Winslow et al., 2016), but 3D modeling is beyond the limitations of the data and the scope of this paper. Two recent studies show the impact of flow perpendicular to the spreading direction (Fisher et al., 2008; Niera et al., 2016), and this caveat should be kept in mind when viewing the results. The likely presence of 3D fluid flow in the natural system does not change the basic conclusion that fluid circulation advects a substantial amount of heat from this system. However, because the dominant fluid flow direction

may not align with seismic line RS-A and our heat flow stations, possible points of fluid recharge and discharge may be located east or west of the seismic line.

4.1 Heat Flow Site PB02

Site PB02, the closest heat flow station to the CRR, is located on ~ 1.6 Ma old oceanic basement where the mean sediment thickness is about 40 m. These 19 heat flow measurements (Table 1) have a mean of 41 mWm^{-2} whereas $q_b \approx 400$ mWm^{-2}. These values yield a mean heat flow deficit, $(1 - q_{obs}/q_b)$, of ≈ 0.9 thereby giving an advective heat flow $q_{adv} \approx 360$ mWm^{-2}. SBI temperatures have a mean and standard deviation of 1.8° and 0.2° C, respectively, implying that upper basement temperatures are homogenized.

Heat flow values observed at PB02 can be grouped broadly into two sets, A and B (Figure 6a). Set A shows uniformly low heat flow, whereas the set B has a southward increasing trend in heat flow suggesting lateral transport of heat by fluid advection (Figure 6a). The possible discharge could be at a sparsely sedimented basement exposure to the south. This interpretation is supported by the two heat flow measurements just south of this basement high that show a northward increasing trend. Recharge could be anywhere in the north as Figure 6b shows continuous thinly-sedimented basement; alternatively, recharge could occur to the east or west of the seismic line. Because SBI temperatures are relatively uniform we apply the well-mixed aquifer model of Langseth & Herman (1981) as outlined in the Appendix B to estimate the lateral mass flow through the basement. The data in set B are well fit by an exponential as shown in Figure 6a which could then be applied in equation (B.2) resulting in a volumetric flow rate per unit length ≈ 415 m^{2}yr^{-1}. Using this flow rate in equation (B.4), enables us to estimate the quantity kh_b; for $h_b = 150$ and 550 m, we obtain permeabilities of $\sim 6 \times 10^{-10}$ and 5×10^{-11} m^2, respectively. These values are similar to those in Figure 5 for $Ra \approx 100Ra_c$. Hence vigorous super-critical convection would largely homogenize the basement temperature distribution, and outcrop to outcrop circulation would transport low temperature fluid laterally and advect heat to the seafloor.

4.2 Heat Flow Site PB03

This site (Figure 7), at a crustal age of 2.6 Ma, consists of 11 measurements (Table 1). The mean sediment thickness is ≈ 70m and mean observed heat flow is 58 mWm^{-2}. The conductive prediction, from equation (1a), is 310 mWm^{-2} yielding a mean heat flow deficit of about 0.82, and an advected heat flow $q_{adv} \approx 260$ mWm^{-2}.

All measurements at PB03, except one, exhibit a uniformly low heat flow. The highest heat flow value of 217 mWm^{-2} appears to occur close to a fault (Figure 7b) that probably serves as a discharge zone. Assuming isothermal upflow through the fault at a temperature T_{sp}, conductive heat flow is expected to decay as $1/x$, where x is the distance from the fault plane. Appendix C outlines the mathematical formulation of this problem. From equation (C.2), with q_b = 217 mWm^{-2} and x = 100 m, we calculate the temperature of the upflow, T_{sp}, in the range of 20 to 35 °C, depending whether we use the basalt or sediment thermal conductivity, respectively (Table 2).

The first six uniformly low heat flow values (from ≈ 83 to 86.5 km in Figure 7a) with the seventh being the highest at this site, suggest lateral advective transport of heat by fluids with the high heat flow point being adjacent to the discharge fault (Figure 7b). Possible recharge could be at a sparsely sedimented basement exposure to the north (Figure 7b). The lateral flow rates through the basement can be estimated by applying the well-mixed aquifer model of Langseth & Herman (1981) as outlined in the Appendix B. From equation (B.1) the quantity uh_b can be estimated, where $dT(x)$ is the T_{sp} calculated using the fault model. This results in uh_b of 1.6 x 10^{-5} m²s^{-1} for T_{sp} =20 °C and 9.2 x 10^{-6} m²s^{-1} for T_{sp} =35 °C. In equation (B.4) using L=5 km (recharge outcrop to discharge fault) enables us to calculate permeabilities, k, and we obtain k = 10^{-10} to 7 x 10^{-11} m² for h_b = 150 m and T_{sp} =20 to 35 °C; and k = 10^{-11} to 7 x 10^{-12} m² for h_b = 550 m and T_{sp} =20 to 35 °C. These values fall in between $Ra \approx 10$ - $100 Ra_c$ (Figure 5).

Given the low estimate of basement temperature, these results suggest that the discharge fault transports most of the advective heat (from $\approx$ 83.5 to 87 km in Figure 5) to the seafloor at this site.

4.3 Heat Flow Site PB04

Site PB04 consists of 15 measurements (Table 1) located on 3.5 Ma crust. The region is covered with sediment having thicknesses ranging from 20 m to 290 m. The measurements are distributed over three sediment ponds with an average heat flow of 42 mWm^{-2}. Equation (1a) yields predicted heat flow of 272 mWm^{-2}, indicating a deficit of about 0.85, or $q_{adv} \approx$ 230 mWm^{-2}.

The measurements at PB04 can be broadly grouped into two sets, C and D (Figure 8a). Set C consists of nine measurements in a sediment pond located between two large topographic highs. Heat flow values in set C have a mean value of 16 mWm^{-2} and display a slightly increasing trend to the south. We interpret these data to reflect outcrop to outcrop lateral heat transfer where recharge occurs at poorly sedimented basement high areas to the north of the pond and discharges through a thinly sedimented basement high to the south. SBI temperatures have a mean and standard deviation of 2.3° and 1.7° C, respectively, implying upper basement temperatures are homogenized. The data are well fit to an exponential as shown in Figure 8a. Hence this fit is applied to equation (B.2) in the well-mixed aquifer model (Appendix B) to estimate the volumetric flow rate per unit length $\approx$ 115 m^{2}yr^{-1}. Applying this flow rate in equation (B.4), we estimate permeabilities of $\sim$ 2 x 10^{-10} and 2 x 10^{-11} m^2 for h_b = 150 m and 550 m, respectively. These values are similar to those for $Ra \approx 100 Ra_c$ (Figure 5). Thus, super-critical buoyancy-driven convection significantly homogenizes the temperature distribution within the basement.

In set D, three measurements are of uniformly low heat flow and one exhibits the highest heat flow of 322 mWm^{-2} at this site. This high heat flow appears to occur close to a fault (Figure 8b) which could serve as a discharge zone. We can use the fault model methodology outlined in Appendix C and used in the analysis of PB03. From equation (C.2), with q_b = 322 mWm^{-2}, we

calculate T$_{sp}$ to be in the range of 25 to 50 °C accounting for thermal conductivity difference between sediment and basement. The estimated temperature of the fluid discharging through the fault is considerably higher than T^{obs}_{SBI}, suggesting that the fault may be tapping warmer fluids from below the upper basement.

Advective heat transfer at site PB04 stems from different environments, and it is not possible to determine the heat loss and the fluid discharge temperature from each site independently. Given the low value of conductive heat flux in group C, we suggest that most the advective loss is associated with outcrop to outcrop circulation.

4.4 Heat Flow Site PB05

The seven heat flow measurements at this site (Table 1) have a mean of 14 mWm^{-2}. The crustal age of 4.5 Ma corresponds to a predicted heat flow (equation (1a)) q_b = 241 mWm^{-2}, indicating a deficit of about 0.94. Thus q_{adv} ~ 230 mWm^{-2}. The average sediment thickness ≈ 120 m except above the large basement mound (Figure 9b), where h_s varies between 0 to 80 m.   From the two-way travel time data, the basement high is approximately 1 km from the base of the sediment layer to the north where the heat flow data were obtained. The sediment thickness at the top of the mound and along its southern flank is negligible. Heat flow increases slightly toward the topographic basement high (Figure 9), suggesting that heat maybe being transferred by advection within it.

If basal heat flow through the basement is 241 mW/m^2, the conductive temperature at the base of the basement high (~ 1km) would be ≈ 120°C, whereas the conductive temperature at the base of the nearby sediment would be ≈ 40°C.   This strong lateral temperature gradient between the sediments and the basement high would drive fluid upward through the basement. From scale analysis, the vertical velocity is given by

$$u_z \sim \frac{\alpha g k \Delta T}{\nu}$$

(4)

Because we do not know whether the advection is sub- or super-critical, we assume the permeability corresponds to $Ra = Ra_c$ in a 550 m thick aquifer. From Figure 5, this value is $\approx 4 \times 10^{-13}$ m^2, yielding $u_z \approx 1.6 \times 10^{-8}$ m/s assuming a mean $\Delta T = 40°C$ driving the flow. If the fluid rising through the basement high exits the sediment-free part of the mound at a typical diffuse flow temperature $\approx 10°C$ (Fisher & Harris, 2010), $q_{adv} = \rho_f c_f u_z \Delta T \approx 640$ mW/m^2, which is approximately 3 times greater than the mean heat flow deficit of ≈ 230 mW/m^2. In order for the total advective heat output through the basement high to balance the observed advective heat flux, the area of advective heat loss in the crust surrounding the basement high would thus need to be approximately three times the area through which advective heat is lost through the basement high. Alternaively, heat advection through the basement high resulting from the lateral temperature gradient may be sub-critical. The permeability of the basement may thus be an order of magnitude, or more, less than estimated assuming $Ra \approx Ra_c$.

4.5 Heat Flow Site PB06

Site PB06 (Figure 10) consists of 15 measurements in 5.7 Ma crust with a mean observed heat flow of 235 mWm^{-2}, slightly higher than the predicted heat flow of 214 mWm^{-2} (Table 1). The sediment thickness averages 145 m, burying the basement. The relative agreement between observed and predicted heat flow is consistent with the thick and continuous sediment cover. Observed heat flow varies between 899 mW m^{-2} over a basement high to 90 mW m^{-2} over the basement low (Figure 10). This variation is greater than can be accounted for with conductive refraction (Von Herzen, 2004). The mean observed basement temperature, $<\Delta T_{SBI}^{obs}> \approx 26$ °C is that expected for this crustal age and sediment thickness, but the variability is larger than can be accounted for with conductive heat flow. Importantly, the SBI temperature is not constant but varies substantially with sediment thickness variations; over the basement high, the sediment

thickness is 19 m and ΔT_{SBI}^{obs} is significantly higher (18.8° C) than predicted (4.4° C). Over basement low, the sediment thickness is 226 m and ΔT_{SBI}^{obs} is significantly lower (29° C) than predicted (52.7 °C). The variability in both heat flow and SBI temperature suggests on going hydrothermal circulation, but because the SBI temperature is not homogenized convection must be sub-critical or only slightly super-critical.

These results suggest upward advective fluid flow in the basement high and downward advective flow in the basement low. These results are similar to those near Hole 504B where heat flow highs occur over bathymetric ridges, basement highs and regions of thin sediment cover, with lows occur over basement lows and regions of thick sediment cover [*Fisher et al.*, 1990, 1994]. Because of the complex interplay of these factors it is difficult to quantify fluid flow rates and basement permeability, but the lateral temperature gradients induced by variations in basement topography and sediment thickness may result in circulation at sub-critical Rayleigh numbers. Sub-critical convection is consistent with the broad spectrum of temperatures at the sediment-basement interface. Assuming that convection in a 550 m thick layer of basement extrusives is at or near the critical number for Rayleigh convection, gives the mean permeability at PB06 of $\sim$ 5 x 10^{-13} m^2.

5. Discussion and Conclusions

The 67 new conductive heat flow measurements collected on the southern flank of the CRR crust between $\approx$ 1.6 and $\approx$ 5.7 Ma, together with legacy data, provide important insights into types and patterns of hydrothermal circulation and advective heat loss from young crust. Comparison between the observed heat flow and the predicted half-space lithospheric cooling model yields a mean heat flow deficit of $\approx$ 70% that is attributed primarily to advective heat transport. Detailed analysis of each site, however, suggests that the magnitude of advective heat transfer (Table 3) is

not a simple function of crustal age. These results provide new insights into hydrothermal circulation mechanisms as conductive heat flow approaches the predicted heat flow curve (Figure 1).

Our analysis indicates that between sites PB02 and PB04 super-critical Rayleigh convection tends to homogenize the basement temperature distribution. Outcrop-to-outcrop circulation (PB02, PB04) and fluid flow through faults (PB03 and PB04), which are superimposed on the Rayleigh convection regime, act to cool the basement by advecting heat to the ocean (Figure 3). At PB05, advective heat loss likely occurs as a result of sub-critical convective flow driven by a significant lateral mean temperature difference between the basement high and surrounding sediments. The advected heat exits through a sediment-free part of the basement high. At PB06, however, there is little evidence of advective heat exchange between the basement and ocean. Thermal convection in the basement is likely sub-critical, driven by differences in basement topography (Figure 3 and 10).

We constructed relatively simple mathematical models and/or used scale analysis for sites PB02-PB05 to understand advective heat flow and estimate the permeability of the upper crust. At PB06 we estimated permeability assuming $Ra \approx Ra_c$. Table 3 lists the estimated permeability at each site, along with that for 6.9 Ma crust near Hole 504B. The results of scale analysis and mathematical modeling points to an order magnitude difference in permeability between the upper 150 m and that of the entire Layer 2A, estimated to be 550 m thick (Table 3). Moreover, the results show that permeability does not decrease monotonically with age, as might be expected from water-rock reactions that tend to fill fracture and pore spaces.

The estimates of basement permeability derived here are not a monotonic function of age. The permeability at site PB03 which has an age of 2.6 Ma appears to be less than at adjacent sites that are both older and younger. Moreover, the estimated crustal permeability drops significantly between PB04 and PB05 (3.5 Ma to 4.5 Ma); and it appears to increase again at PB06. At Hole 504B

at 6.9 Ma crust, packer measurements yield permeabilities in the range of 10^{-13} to 10^{-14} m^2 (Anderson & Zoback, 1982; Fisher *et al.* 1990) and flow-based determinations produce upper basement permeabilities of 1-5 x 10^{-14} m^2 (Becker *et. al.* 2004). At Hole 896A, located 1 km from Hole 504B, drill-string packer measurements (Becker, 1996) and flow-based determinations (Becker *et. al.* 2004) give upper basement permeabilities of 1-4 x 10^{-13} m^2 and lower basement permeability of 2 x 10^{-14} m^2. However, the near uniformity of basement temperature between Hole 504B, Hole 896A and Holes 677, 678, despite large differences in sediment thickness, suggest vigorous convection in the upper crustal layer. Davis *et al.* (2004) suggest a model-based regional-scale permeability of $\sim 10^{-9}$ m^2 in the upper 100 m. The substantial transition to decreased permeabilities, from 3.5 to 4.5 Ma and a continued decrease in permeability in the shallow crust at 6.9 Ma suggests that the evolution of crustal permeability may not be simply correlated with crustal age.

The variability in estimated crustal permeabilities is similar to the variability seen in tomographic models of seismic p-wave velocity in Layer 2A of the ocean crust (Wilson *et al.* 2019). The upper oceanic crust older than about 5.7 Ma consistently shows a higher seismic velocity that is interpreted to be a result of porosity reduction (Gregory *et al.* 2019; Wilson et al., 2019). The crust younger than 5.7 Ma can be segmented into regions characterized by a combination of basement roughness, seismic velocity of Layer 2A & 2B, and ages determined from reinterpretation of magnetic anomaly data (Wilson *et al.* 2019). Taken together, these characteristics suggest that the magma supply has waxed and waned with time. Heat flow measurements at sites PB02 and PB03 lie in a region where the tomography model indicates a lower velocity Layer 2A, which is consistent with the relatively high permeability estimated for this region. Sites PB04 and PB05 are located in a region of variable p-wave velocities in Layer 2A. Wilson et al. (2019) suggests that this region has formed during a period of slower spreading, < 35 mm/yr half-rate, with enhanced faulting accommodating part of the extension. This may explain the rapid change in estimated permeability.

Site PB06 and Hole 504B lie within the transition to significantly faster Layer 2A velocities, which are interpreted to indicate an earlier phase of magma-dominated spreading.

The models used to analyze the heat flow data along the seismic line from crustal ages of ≈1.6 to ≈ 5.7 Ma are necessarily simplified. In addition, the models all assume 2D flow parallel to the spreading direction, whereas enhanced permeability may be aligned parallel to the ridge (Fisher *et al.* 2008; Neira *et. al.* 2016), Outcrop to outcrop flow may also be 3D (Winslow & Fisher, 2015; Winslow *et. al.*, 2016), and fault-controlled flow may be both along and perpendicular to the plane of the fault (e.g., Johnson *et. al.*, 1993; Lowell, 2017). The permeability values estimated for the various sites represent bulk average permeabilities. The estimated values obtained are large, indicating that the permeability is probably fracture controlled, and the actual flow paths may be both anisotropic and defined by a few major fractures rather than by Darcy flow as used here.

Figure 1b shows that heat flow at sites PB02 thru PB05 lies well below the predicted cooling curve but begin climbing towards the cooling curve at ≈ 4.5 Ma, essentially reaching the curve at 5.7 Ma. This result is in contrast with the global data set (Figure 1a) where heat flow coincides with the predicted heat flow at ≈ 65 ± 10 Ma. Stein & Stein (1994) argue that the coincidence of conductive heat flow with the predicted cooling curve suggests that hydrothermal circulation is weak as a result of decreasing crustal permeability rather than a result of increasing sediment thickness burying basement rock. This study, where heat flow coincides with the cooling curve at a much younger crustal age of ≈ 5.7 Ma, however, indicates that the alignment of heat flow with the predicted curve may be a function of original permeability at the time of crustal formation or reduction of permeability, which may result from mineral precipitation as well as mode of crustal generation, as well as sediment accumulation. The data at PB05 and PB06 indicate that a decline in crustal permeability results in sub-critical or weakly super-critical convection, driven largely by basement topography. The relatively thick, low permeability sediment cover over crust older than

about 5.7 Ma inhibits advective heat transfer to the ocean (Figure 3). This is similar to the JDFR flank where thick sediment cover also inhibits advective heat loss from young crust (Davis *et al.* 1997; Davis *et. al.*, 1999; Spinelli & Fisher, 2004; Hutnak *et. al.*, 2006).

The results of studies at young crust thus suggest that permeability, sediment thickness, topographical structure and variations in tectonic and magmatic activities with age all affect hydrothermal circulation in the oceanic crust in a complex interconnected fashion. This interconnectedness is more site specific than that can be constrained by global datasets and models simply as a function of age. Increased understanding of crustal evolution and hydrothermal circulation will come as individual spreading systems are analyzed that includes details of crustal creation, tectonic evolution, water rock reactions, sedimentation, and age.

Appendix A: 1-D Thermal Conduction Model

To estimate the expected temperature at the sediment-basement interface, we construct a 1-D steady state layered thermal conduction model consisting of a uniform layer of sediment overlying basaltic basement. We assume that thermal conductivity of each layer is constant, implying that,

$$\frac{d^2T}{dz^2} = 0$$

(A.1)

where T is temperature and z is depth, subject to the conditions:

$$T_s(z=0) = T_{sw}$$
$$\lambda_b \frac{dT_b}{dz}\bigg|_{z=h_b} = q_b$$

(A.2)

Definitions and values of symbols are given in Table 2. Temperature and heat flux are continuous across the sediment –basement interface. Consequently, in the sediment layer,

$$T_S(z) = T_{sw} + \frac{q_b}{\lambda_s}z; \, 0 \leq z \leq h_s$$

(A.3)

and the temperature at the sediment basement interface, relative to T_{sw} is

$$\Delta T_{SBI}(h_s) = \frac{q_b h_s}{\lambda_s}$$

(A.4)

Applying the half space cooling model in equation (1a) and assuming a constant sedimentation rate $h_s = v_s\tau$, we derive equation (2).

Appendix B: The Well-Mixed Aquifer Model

To estimate the lateral mass flow through the basement, we apply the well-mixed aquifer model of *Langseth and Herman* (1981) (Figure B1), where lateral advection dominates heat transport by conduction. The steady state thermal balance is expressed as,

$$\rho_f c_f u h_b \frac{dT(\mathrm{x})}{dx} = q_b - \lambda_s \frac{T(x)}{h_s} \tag{B.1}$$

The exponential solution to this equation by applying boundary conditions $T = T_0$ at $x = x_0$ yields (*Kolandaivelu et al.* 2017),

$$\frac{q(x)}{q_b} = 1 + \left(\frac{q(x_0)}{q_b} - 1\right)\left[e^{\frac{a^*}{u h_b h_s}(x_0 - x)}\right] \tag{B.2}$$

For parameters shown in this appendix, refer to Table 2. Here $a^* = \lambda s/\rho_f c_f$; $q(x)$ is heat flow at distance of x from x_0; $q(x_0)$ is the heat flow at distance x_0; x_0 is the distance of the first heat flow measurement from the recharge outcrop (Table 1). An exponential fit based on the observed data and equating it to exponential in equation (B.2) provides the volumetric flow rate per unit length perpendicular to the flow direction, $u h_b$ for a sediment thickness, h_s. Extrapolating the exponential fit to the data to the presumed discharge location from first measurement, heat flow at discharge, q_d, can be estimated and writing,

$$q_d = \lambda_s \frac{T_d}{h_s} \tag{B.3}$$

yields T_d and therefore is the ΔT_r as recharge is assumed to occur at 0 °C.

Darcy's law can be modified and expressed as,

$$u h_b = \frac{\alpha g k \Delta T_r h_b (h_b + h_s)}{\nu L} \tag{B.4}$$

This expression enables estimating formation permeability, kh_b. Substituting the calculated values from equations (B.2) and (B.3), we can arrive at permeabilities, k, for h_b = 150 m and 550 m.
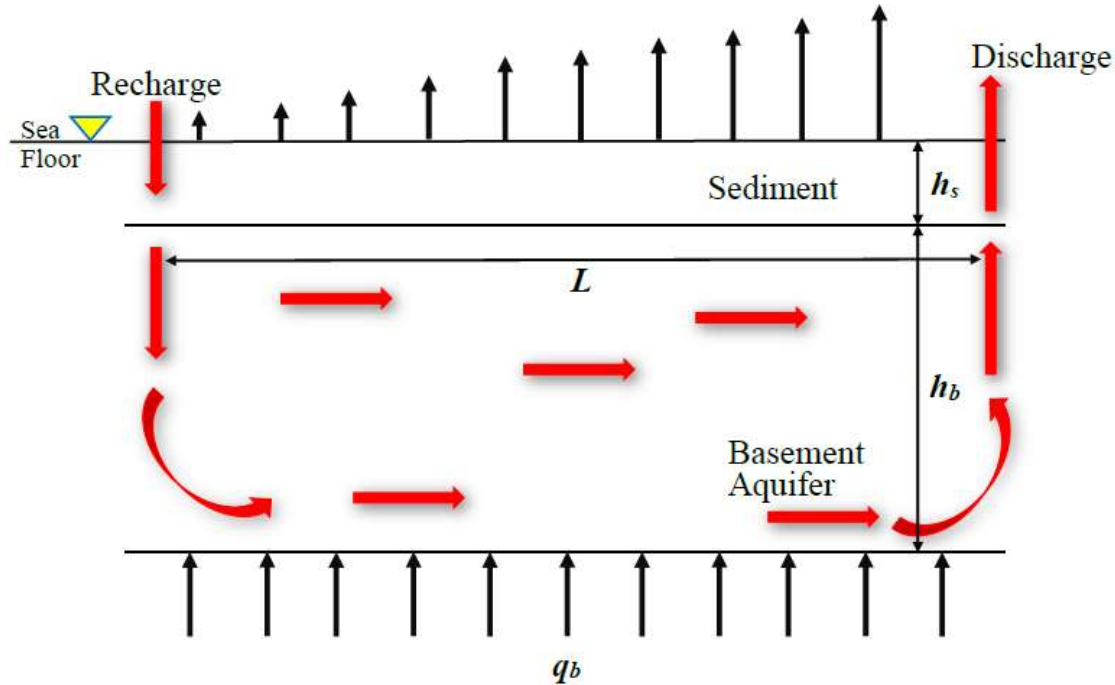

Figure B1. A well-mixed aquifer flow model modified from *Langseth and Herman*, 1981. Refer to Table 2 for parameters shown in this figure.

Appendix C: Heat flow near a fault

To consider how conductive heat flow changes near a fault, we follow the approach outlined in *Lowell* (1975) in which the fault was modeled as vertical plane of height h and a constant temperature T_{sp}, placed at $x = 0$. Then assuming the seafloor is a horizontal plane $z = 0$, maintained at temperature $T = 0$, the steady state temperature distribution in the rock adjacent to the fault can be found as outlined in *Carslaw and Jaeger* (1959). That is:

$$T(x,z) = \frac{T_{sp}}{\rho}\left[2\tan^{-1}\frac{z}{x} - \tan^{-1}\frac{z-h}{x} - \tan^{-1}\frac{z+h}{x} \right] \qquad \text{(C.1)}$$

The conductive heat flux at the surface $z = 0$ is then:

$$q = \frac{2T_{sp}l_s}{p}\left[\frac{1}{x} - \frac{x}{x^2 + h^2}\right] \qquad (C.2)$$

If $x << h$, the second term in equation (C.2) may be neglected.

References

Alt, J. C., 1995. Sulfur isotopic profile through the oceanic crust: Sulfur mobility and seawater-crustal sulfur exchange during hydrothermal alteration, *Geology*, 23(7), 585-588.

Anderson, B. W., Coogan, L. A., & Gillis, K. M., 2012. The role of outcrop- to- outcrop fluid flow in off- axis oceanic hydrothermal systems under abyssal sedimentation conditions, *J. Geophys. Res.*, 117(B5).

Anderson, R. N., & Hobart, M. A., 1976. The relation between heat flow, sediment thickness, and age in the eastern Pacific, *J. Geophys. Res.*, 81(17), 2968-2989.

Anderson, R. N., & Zoback, M. D., 1982. Permeability, underpressures, and convection in the oceanic crust near the Costa Rica Rift, eastern equatorial Pacific, *J. Geophys. Res.*, 87(B4), 2860-2868.

Baker, P. A., Stout, P. M., Kastner, M., & Elderfield, H., 1991. Large-scale lateral advection of seawater through oceanic crust in the central equatorial Pacific, *Earth Planet. Sci. Letters,* 105(4), 522-533.

Becker, K., 1985. Large-scale electrical resistivity and bulk porosity of the oceanic crust, Deep Sea Drilling Project Hole 504B, Costa Rica Rift. In *Initial reports DSDP, Leg 83, Balboa to Balboa, Panama*. US Govt. Printing Office; UK distributors, IPOD Committee, NERC, Swindon.

Becker, K., Sakai, H., Adamson, A. C., Alexandrovich, J., Alt, J. C., Anderson, R. N., ... & Ishizuka, H., 1989. Drilling deep into young oceanic crust, Hole 504B, Costa Rica Rift, *Rev. Geophy.*, 27(1), 79-102.

Becker, K., 1996. Permeability measurements in Hole 896A and implications for the lateral variability of upper crustal permeability at Sites 504 and 896. In *PROCEEDINGS-OCEAN DRILLING PROGRAM SCIENTIFIC RESULTS* (pp. 353-364). NATIONAL SCIENCE FOUNDATION.

Becker, K., & Davis, E. E., 2004. In situ determinations of the permeability of the igneous oceanic crust, *Hydrogeo. Oceanic Lithosphere*, 189-224. Edited by E. E. Davis and H. Elderfield, Cambridge Univ. Press, New York.

Becker, K., Davis, E.E. and Spiess, F.N., 2004. Temperature and video logs from the upper oceanic crust, Holes 504B and 896A, Costa Rica Rift flank: implications for the permeability of upper oceanic crust. *Earth and Planetary Science Letters*, *222*(3-4), pp.881-896.

Carslaw, H. S., & Jaeger, J. C., 1959. Conduction of heat in solids, *Oxford: Clarendon Press,* 2nd ed.

Carlson, R. L., 2011. The effect of hydrothermal alteration on the seismic structure of the upper oceanic crust: Evidence from Holes 504B and 1256D, *Geochem. Geophy. Geosys.*, 12(9). Carlson, R. L., 2014. The effects of alteration and porosity on seismic velocities in oceanic basalts and diabases, *Geochem. Geophy. Geosys.*, 15(12), 4589-4598.

Cherkaoui, A. S., Wilcock, W. S., Dunn, R. A., & Toomey, D. R., 2003. A numerical model of hydrothermal cooling and crustal accretion at a fast spreading mid-ocean ridge, *Geochem. Geophy. Geosys.*, 4(9).

Craft, K. L., & Lowell, R. P., 2009. A boundary layer model for submarine hydrothermal heat flows at on- axis and near- axis regions, *Geochem. Geophy. Geosys.*, 10(12).

Davies, J. H., & Davies, D. R., 2010. Earth's surface heat flux, *Solid Earth*, 1(1), 5.

Davis, E. E., Fisher, A. T., Firth, J. V., Staff Scientist, L., Fox, P. J., Allan, J., ... & Home, O. D. P., 1997. Hydrothermal circulation in the oceanic crust: Eastern flank of the Juan de Fuca Ridge, In *Proc. ODP Initial Reports*, 168, 1-470.

Davis, E. E., Chapman, D. S., Wang, K., Villinger, H., Fisher, A. T., Robinson, S. W., ... & Becker, K., 1999. Regional heat flow variations across the sedimented Juan de Fuca Ridge eastern flank: Constraints on lithospheric cooling and lateral hydrothermal heat transport, *J. Geophys. Res.*, 104(B8), 17675-17688.

Davis, E. E., Wang, K., Becker, K., Thomson, R. E., & Yashayaev, I., 2003. Deep- ocean temperature variations and implications for errors in seafloor heat flow determinations, *J. Geophys. Res.*, 108(B1).

Davis, E. E., Becker, K., & He, J., 2004. Costa Rica Rift revisited: constraints on shallow and deep hydrothermal circulation in young oceanic crust, *Earth Planet. Sci. Letters*, 222(3-4), 863-879.

Elder, J. W. (1965). Physical processes in geothermal areas, *Terrestrial heat flow*, *Geophysical Monograph Series,* 8, edited by W.H.K. Lee, p. 211-239, AGU, Washington, D.C.

Elderfield, H., & Schultz, A., 1996. Mid-ocean ridge hydrothermal fluxes and the chemical composition of the ocean, *Ann. Rev. Earth Planet. Sci.*, 24(1), 191-224.

Embley, R. W., Hobart, M. A., Anderson, R. N., & Abbott, D., 1983. Anomalous heat flow in the northwest Atlantic: A case for continued hydrothermal circulation in 80- MY crust, *J. Geophys. Res.,* 88(B2), 1067-1074.

Fisher, A. T., 1998. Permeability within basaltic oceanic crust, *Rev. Geophy.*, 36(2), 143-182.

Fisher, A.T., 2003, Geophysical constraints on hydrothermal circulation: observations and models, in: P.E. Halbach, V. Tunnicliffe, J.R. Hein (Eds.), Energy and Mass Transfer in Marine Hydrothermal Systems, vol. 89, *Dahlem University Press*, 29 – 52

Fisher, A. T., Becker, K., Narasimhan, I. T. N., Langseth, M. G., & Mottl, M. J., 1990. Passive, off- axis convection through the southern flank of the Costa Rica Rift, *J. Geophys. Res.*, 95(B6), 9343-9370.

Fisher, A. T., Becker, K., & Narasimhan, T. N., 1994. Off- axis hydrothermal circulation: Parametric tests of a refined model of processes at Deep Sea Drilling Project/Ocean Drilling Program site 504, *J. Geophys. Res.,* 99(B2), 3097-3121.

Fisher, A. T., & Becker, K., 2000. Channelized fluid flow in oceanic crust reconciles heat-flow and permeability data, *Nature*, 403(6765), 71-74.

Fisher, A.T., Stein, C.A., Harris, R.N., Wang, K., Silver, E.A., Pfender, M., Hutnak, M., Cherkaoui, A., Bodzin, R. and Villinger, H., 2003a. Abrupt thermal transition reveals hydrothermal boundary and role of seamounts within the Cocos Plate. *Geophysical Research Letters*, *30*(11).

Fisher, A. T., Davis, E. E., Hutnak, M., Spiess, V., Zühlsdorff, L., Cherkaoui, A., ... & Mottl, M. J., 2003b. Hydrothermal recharge and discharge across 50 km guided by seamounts on a young ridge flank, *Nature*, 421(6923), 618-621.

Fisher, A.T. and Von Herzen, R.P., 2005. Models of hydrothermal circulation within 106 Ma seafloor: Constraints on the vigor of fluid circulation and crustal properties, below the Madeira Abyssal Plain. *Geochemistry, Geophysics, Geosystems*, *6*(11).

Fisher, A. T., Davis, E. E., and Becker, K., 2008, Borehole-to-borehole hydrologic response across 2.4 km in the upper oceanic crust: Implications for crustal-scale properties, *J. Geophys. Res.,* 113, B07106.

Fisher, A. T., & Harris, R. N., 2010. Using seafloor heat flow as a tracer to map subseafloor fluid flow in the ocean crust, *Geofluids*, 10(1- 2), 142-160.

Gregory, E. P. M., Hobbs, R. W., Peirce, C., & Wilson, D. J., 2018. 2B or not 2B? – a terminology-independentproxy for characterising the extrusive-intrusive transition in magmatic oceanic crust, *Geochem. Geophy. Geosys.(submitted).*

Hasenclever, J., Theissen-Krah, S., Rüpke, L. H., Morgan, J. P., Iyer, K., Petersen, S., & Devey, C. W., 2014. Hybrid shallow on-axis and deep off-axis hydrothermal circulation at fast-spreading ridges, *Nature*, 508(7497), 508-512.

Hasterok, D., 2013. A heat flow based cooling model for tectonic plates, *Earth Planet. Sci. Letters*, 361, 34-43.

Heberling, C., Lowell, R. P., Liu, L., & Fisk, M. R., 2010. Extent of the microbial biosphere in the oceanic crust, *Geochem. Geophy. Geosys.*, 11(8), Q08003.

Hobart, M. A., Langseth, M. G., & Anderson, R. N., 1985. A geothermal and geophysical survey on the south flank of the Costa Rica Rift: sites 504 and 505, *Initial Reports of the Deep Sea Drilling Project*, 83(APR), 379-404.

Huber, J. A., Butterfield, D. A., & Baross, J. A., 2003. Bacterial diversity in a subseafloor habitat following a deep-sea volcanic eruption, *FEMS Microbiology Ecology*, 43(3), 393-409.

Hutchison, I., 1985. The effects of sedimentation and compaction on oceanic heat flow, *Geophys. Jour. Inter.*, 82(3), 439-459.

Hutnak, M., Fisher, A. T., Zühlsdorff, L., Spiess, V., Stauffer, P. H., & Gable, C. W., 2006. Hydrothermal recharge and discharge guided by basement outcrops on 0.7–3.6 Ma seafloor east of the Juan de Fuca Ridge: Observations and numerical models, *Geochem. Geophy. Geosys.*, 7(7). Q7002.

Hutnak, M., & Fisher, A. T., 2007. Influence of sedimentation, local and regional hydrothermal circulation, and thermal rebound on measurements of seafloor heat flux, *J. Geophys. Res.,* , 112 (B12).

Hutnak, M., Fisher, A. T., Harris, R., Stein, C., Wang, K., Spinelli, G., ... & Silver, E., 2008. Large heat and fluid fluxes driven through mid-plate outcrops on ocean crust, *Nature Geoscience*, 1(9), 611-614.

Hyndman, R.D., Davis, E.E. and Wright, J.A., 1979. The measurement of marine geothermal heat flow by a multipenetration probe with digital acoustic telemetry and in situ thermal conductivity, *Marine Geophysical Researches*, 4(2), 181-205.

Jarrard, R. D., Abrams, L. J., Pockalny, R., Larson, R. L., & Hirono, T., 2003. Physical properties of upper oceanic crust: Ocean Drilling Program Hole 801C and the waning of hydrothermal circulation, *J. Geophys. Res.,* 108(B4).

Johnson, H. P., Becker, K., & Von Herzen, R., 1993. Near- axis heat flow measurements on the northern Juan de Fuca Ridge: Implications for fluid circulation in oceanic crust, *Geophy. Res. Lett.*, 20(17), 1875-1878.

Kolandaivelu, K. P., Harris, R. N., Lowell, R. P., Alhamad, A., Gregory, E. P., & Hobbs, R. W., 2017. Analysis of a conductive heat flow profile in the Ecuador Fracture Zone, *Earth Planet. Sci. Letters*, 467, 120-127.

Langseth, M. G., & Von Herzen, R. P., 1970. Heat flow through the floor of the world oceans, *The sea*, 4(part 1), 299-352.

Langseth, M. G., & Herman, B. M., 1981. Heat transfer in the oceanic crust of the Brazil Basin, *J. Geophys. Res.,* , 86(B11), 10805-10819. 05

Langseth, M. G., Cann, J. R., Natland, J. H., & Hobart, M., 1983. Geothermal phenomenon at the Costa Rica Rift: background and objectives for drilling at Deep Seas Drilling Project sites 501, 504, and 505, *Initial reports of the Deep Sea Drilling Project*, 69(MAY), 5-30.

Langseth, M. G., Mottl, M. J., Hobart, M. A., & Fisher, A., 1988. The distribution of geothermal and geochemical gradients near Site 501/504: implications for hydrothermal circulation in the oceanic crust, In *Proc. Ocean Drill. Program Initial Rep*, 111, 23-32.

Langseth, M. G., Becker, K., Von Herzen, R. P., & Schultheiss, P., 1992. Heat and fluid flux through sediment on the western flank of the Mid- Atlantic Ridge: A hydrogeological study of North Pond, *Geophy. Res. Lett.*, 19(5), 517-520.

Lister, C. R. B., 1972. On the thermal balance of a mid-ocean ridge, *Geophys. Jour. Inter.*, 26(5), 515-535.

Lister, C. R. B., 1982. "Active" and "passive" hydrothermal systems in the oceanic crust: predicted physical conditions, *The dynamic environment of the ocean floor*, 441-470. ed. By K. Fanning and F.T. Manheim, D.C. Hearth, Lexington, MA.

Lonsdale, P. and Klitgord, K.D., 1978. Structure and tectonic history of the eastern Panama Basin. *Geological Society of America Bulletin*, *89*(7), 981-999.

Lowell, R. P., 1975. Circulation in fractures, hot springs, and convective heat transport on mid-ocean ridge crests, *Geophys. Jour. Inter.*, 40(3), 351-365.

Lowell, R. P., & Germanovich, L. N., 2004. Hydrothermal processes at mid- ocean ridges: Results from scale analysis and single- pass models, *Mid-Ocean Ridges: Hydrothermal Interactions Between the Lithosphere and Oceans, Geophysical Monographic Series,* 148, 219-244. ed. by C.R. German, J. Lin, and L.M. Parson, AGU, Washington, D. C.

Lowell, R. P., 2017. A fault- driven circulation model for the Lost City Hydrothermal Field, *Geophy. Res. Lett.*, 44(6), 2703-2709.

Macdonald, K. C., 1982. Mid-ocean ridges: Fine scale tectonic, volcanic and hydrothermal processes within the plate boundary zone, *Ann. Rev. Earth Planet. Sci.*, 10(1), 155-190.

Neira, N.M., Clark, J.F., Fisher, A.T., Wheat, C.G., Haymon, R.M. and Becker, K., 2016. Cross-hole tracer experiment reveals rapid fluid flow and low effective porosity in the upper oceanic crust. *Earth and Planetary Science Letters*, *450*, pp.355-365.

Nield, D. A., 1968. Onset of thermohaline convection in a porous medium, *Water Resources Research*, 4(3), 553-560.

Parsons, B. and Sclater, J.G., 1977. An analysis of the variation of ocean floor bathymetry and heat flow with age. *Journal of geophysical research*, *82*(5), pp.803-827.

Cheng, Q., 2016. Fractal density and singularity analysis of heat flow over ocean ridges, *Scientific reports,* 6, 19167.

Salisbury, M.H., Christensen, N.I., Becker, K. and Moos, D., 1985. The velocity structure of Layer 2 at Deep Sea Drilling Project Site 504 from logging and laboratory experiments. *Unknown Journal*, pp.529-539.

Sclater, J., Jaupart, C., & Galson, D., 1980. The heat flow through oceanic and continental crust and the heat loss of the Earth, *Rev. Geophy.*, 18(1), 269-311.

Spinelli, G. A., & Fisher, A. T., 2004. Hydrothermal circulation within topographically rough basaltic basement on the Juan de Fuca Ridge flank. *Geochem. Geophy. Geosys.*, 5(2).

Spinelli, G. A., & Harris, R. N., 2011. Effects of the legacy of axial cooling on partitioning of hydrothermal heat extraction from oceanic lithosphere, *J. Geophys. Res.,* 116(B9), B09102.

Stein, C. A., & Stein, S., 1992. A model for the global variation in oceanic depth and heat flow with lithospheric age, *Nature*, 359(6391), 123-129.

Stein, C. A., & Stein, S., 1994. Constraints on hydrothermal heat flux through the oceanic lithosphere from global heat flow, *J. Geophys. Res.,* 99(B2), 3081-3095.

Stein, J. S., & Fisher, A. T., 2001. Multiple scales of hydrothermal circulation in Middle Valley, northern Juan de Fuca Ridge: Physical constraints and geologic models, *J. Geophys. Res.,* 106(B5), 8563-8580.

Theissen-Krah, S., Iyer, K., Rüpke, L. H., & Morgan, J. P., 2011. Coupled mechanical and hydrothermal modeling of crustal accretion at intermediate to fast spreading ridges, *Earth Planet. Sci. Letters*, 311(3-4), 275-286.

Villinger, H., & Davis, E. E., 1987. A new reduction algorithm for marine heat flow measurements, *J. Geophys. Res.*, 92(B12), 12846-12856.

Von Herzen, R. P., 2004. Geothermal evidence for continuing hydrothermal circulation in older (> 60 Ma) ocean crust, *Hydrogeology of the Oceanic Lithosphere*, 414-450.

Wheat, C. G., Mottl, M. J., Fisher, A. T., Kadko, D., Davis, E. E., & Baker, E., 2004. Heat flow through a basaltic outcrop on a sedimented young ridge flank, *Geochem. Geophy. Geosys.*, 5(12).

Williams, D. L., & Von Herzen, R. P., 1974. Heat loss from the Earth: new estimate, *Geology*, 2(7), 327-328.

Wilson, D. S., & Hey, R. N., 1995. History of rift propagation and magnetization intensity for the Cocos- Nazca sspreading Center, *J. Geophys. Res.,* 100(B6), 10041-10056.

Wilson, D.S., D. A. H. Teagle, G. D. Acton, et al., 2003. *Proc. ODP, Init. Repts., 206:* College Station, TX (Ocean Drilling Program).

Wilson, Dean, Richard Hobbs, Christine Peirce, Emma Gregory, and Adam Robinson. "Intermediate oceanic crust is created by alternating periods of magma-rich and magma-poor spreading: evidence from a 7 Myr transect from the Costa Rica Ridge to ODP borehole 504B." In EGU General Assembly Conference Abstracts, vol. 20, p. 15604. 2018.

Winslow, D. M., & Fisher, A. T., 2015. Sustainability and dynamics of outcrop-to-outcrop hydrothermal circulation, *Nature communications*, 6, 7567.

Winslow, D. M., Fisher, A. T., Stauffer, P. H., Gable, C. W., & Zyvoloski, G. A., 2016. Three- dimensional modeling of outcrop- to- outcrop hydrothermal circulation on the eastern flank of the Juan de Fuca Ridge, *J. Geophys. Res.,* 121(3), 1365-1382.

Worm, H.U., Böhm, V. and Bosum, W., 1996. 24. IMPLICATIONS FOR THE SOURCES OF MARINE MAGNETIC ANOMALIES DERIVED FROM MAGNETIC LOGGING IN HOLES 504B AND 896A1. In *Proceedings of the Ocean Drilling Program: Scientific results* (p. 331). The Program.
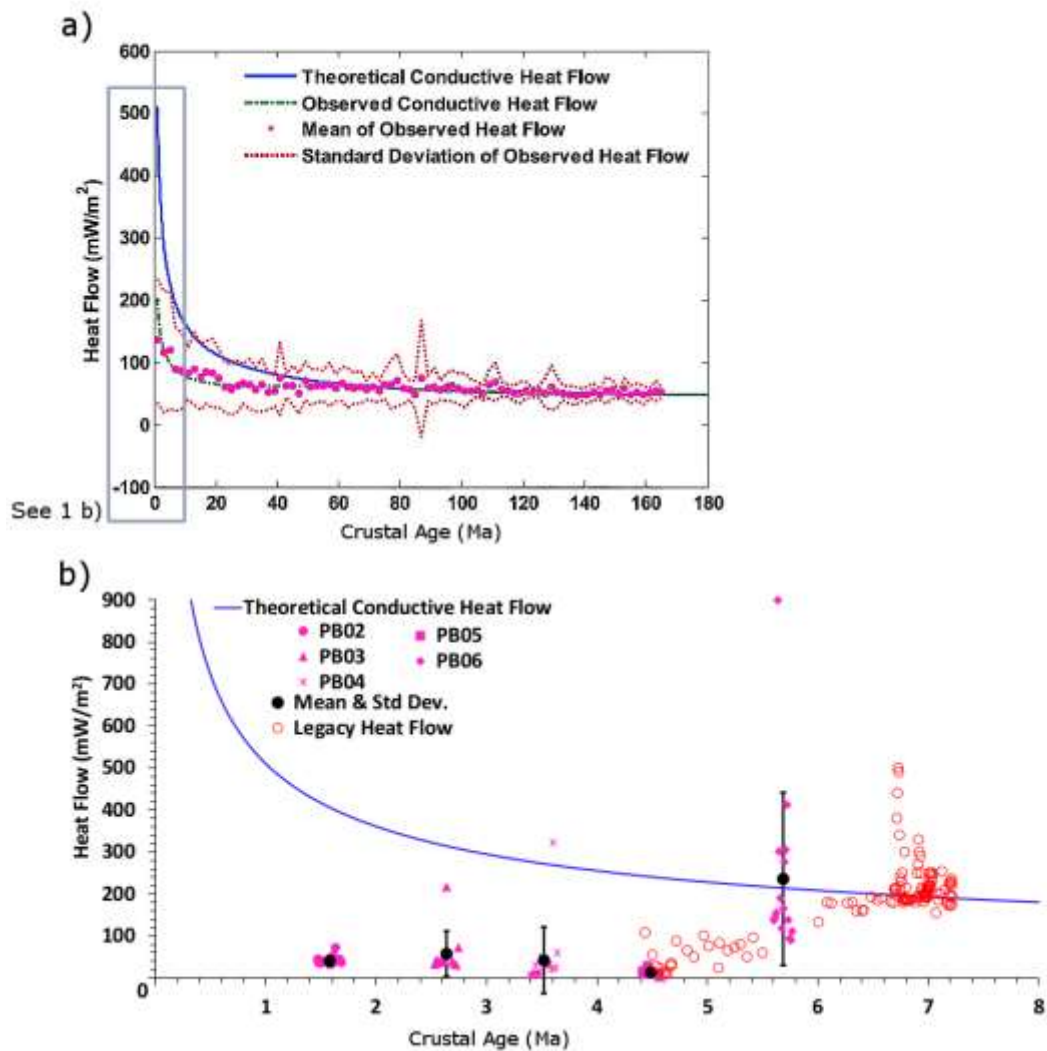
Figure 1. a) Conductive heat loss as a function of oceanic crustal age. Blue line shows predicted fit using equation 1a. The pink dots are observed data averaged in 2 Ma bins; red dotted lines show standard deviation; green dotted-dashed line show fit to the binned data (from *Heberling et al.* 2010). b) Heat flow on the south flank of the Costa Rica Rift as a function of oceanic crustal age. Blue line shows predicted fit/conductive cooling curve from equation 1a. Solid pink symbols are 67 new heat flow measurements divided into five sites (PB02 at 1.6 Ma; PB03 at 2.6 Ma; PB04 at 3.5 Ma; PB05 at 4.5 Ma and PB06 at 5.7 Ma) in this study along with their mean and standard deviation in black. Red open circles show legacy heat flow data (*Anderson and Hobart,* 1976; *Langseth et al.* 1983, 1988; *Hobart et al.* 1985; *Davis et al.* 2003, 2004). Note that the legacy heat flow values are projected laterally up to 10 km onto the profile in Figure 1b.
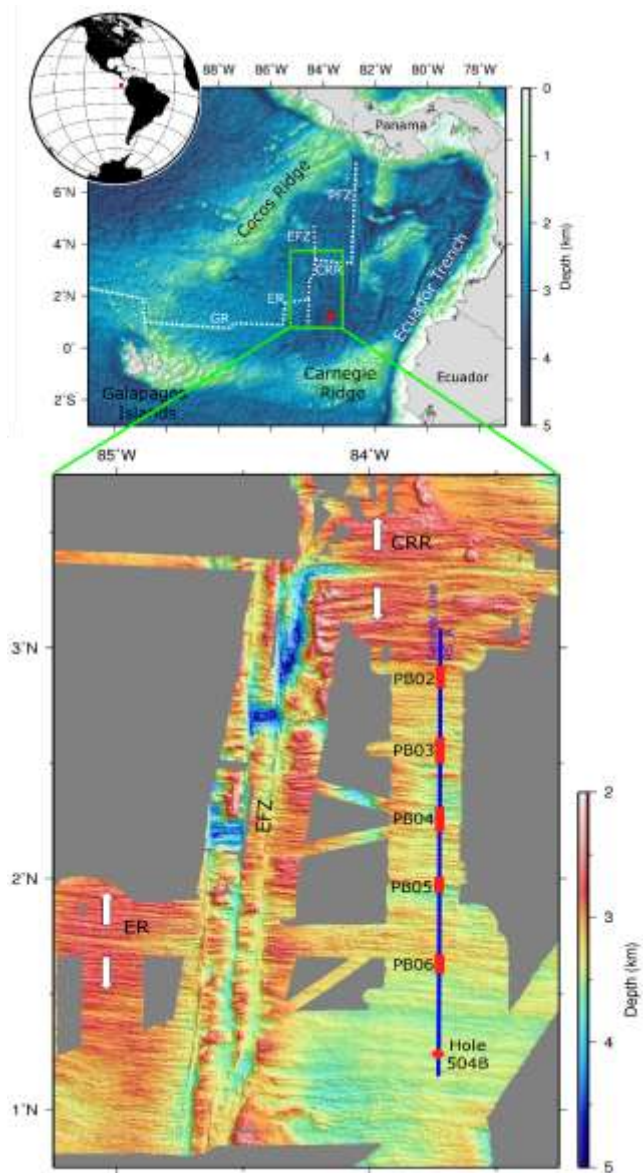
Figure 2. Location and bathymetry of the Panama Basin. The top panel gives the regional context for the Panama Basin. The basin is bounded by the Cocos Ridge to the N and W, the Carnegie Ridge to the S, and the Ecuador Trench and Americas to the E. Dashed white lines show the spreading axis (CRR = Costa Rica Rift; ER = Ecuador Ridge; GR = Galapagos Spreading Center). Transforms bounding the CRR, EFZ = Ecuador Fracture Zone; PFZ = Panama Fracture Zone, are labeled. Red diamond shows the location of the ODP Hole 504B. Green box encloses the area where geophysical measurements were made during cruises JC112, JC113 and Sonne 0238. Bottom panel shows a zoom in of the green box with the spreading direction of the rifts shown in white arrows. RS_A seismic profile spanning from slightly north of the first heat flow site, PB02, to beyond ODP Hole 504B is shown in the blue line. Stations PB02 to PB05 on RS_A are shown as red solid rectangles.
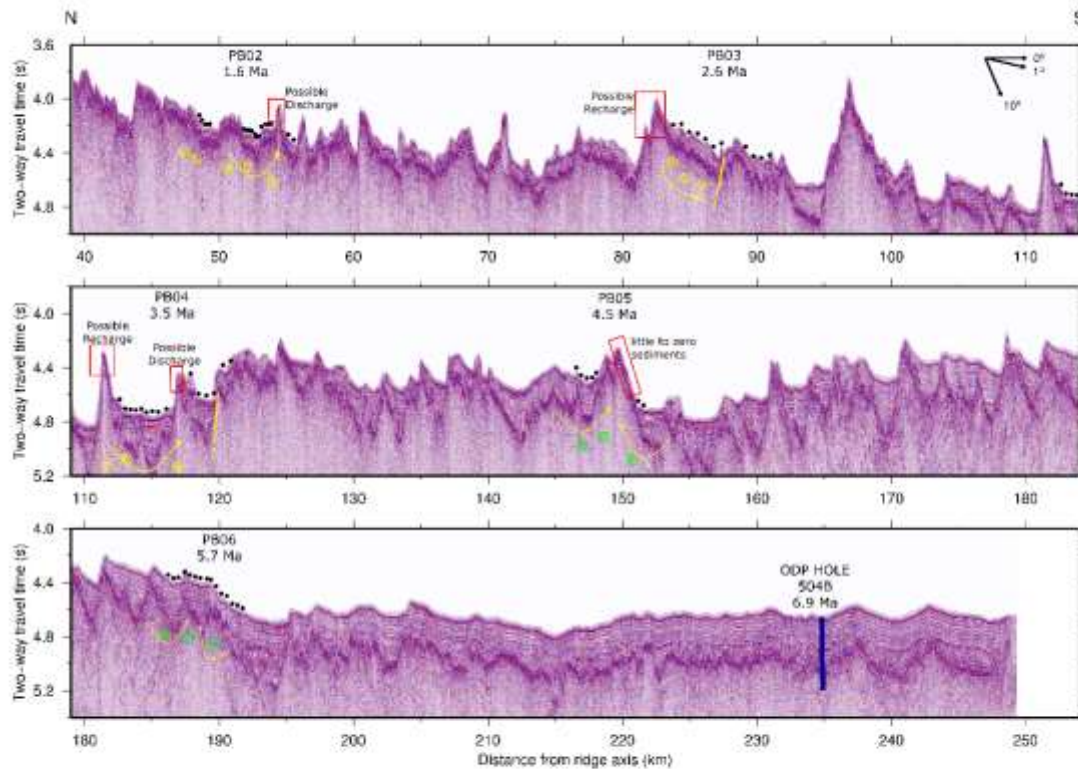
Figure 3. Pre-stack time migrated seismic image (RS_A seismic profile) showing heat flow stations PB02 through PB06 and ODP Hole 504B as a function of the distance from the Costa Rica Rift. Heat flow stations PB02 through PB06 and their various heat transport mechanisms are shown. The curved yellow arrows indicate outcrop to outcrop type circulations except at PB06 where they indicate heat flow focused around buried basement highs. The yellow spirals indicate super-critical convection cells that homogenize basement temperatures. The green spirals in PB05 and PB06 indicate sub- to slightly super-critical convection which redistributes heat. The yellow parallel lines and arrows (PB03 and PB04) indicate upflow of fluids through a fault. N=North and S=South.
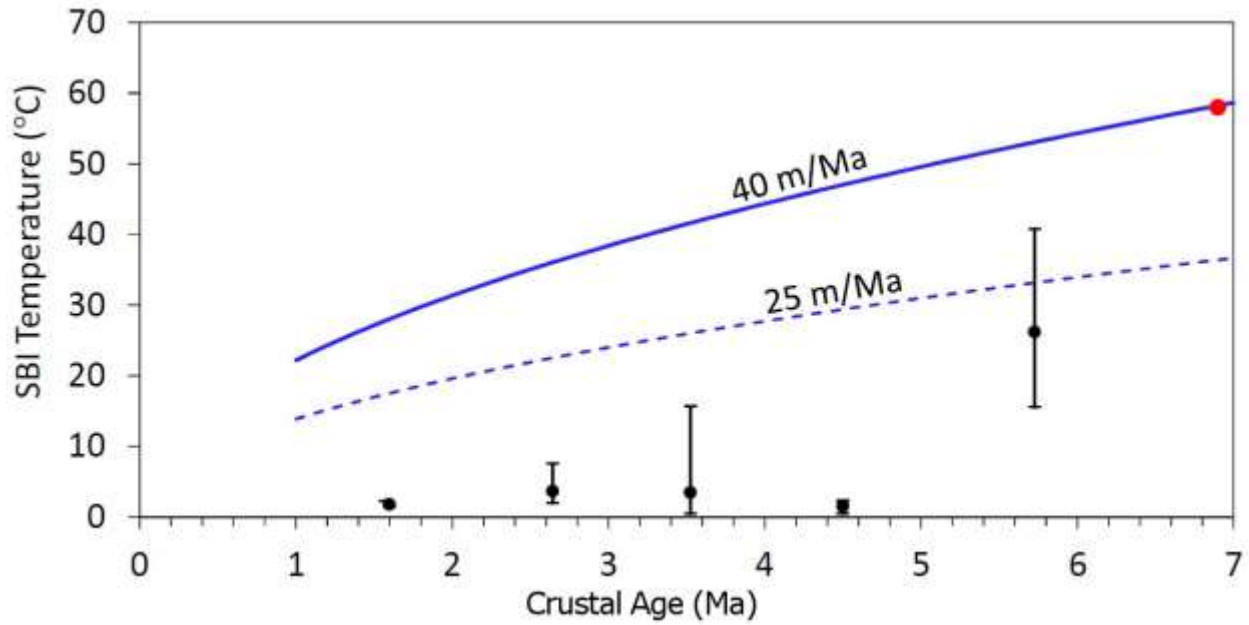
Figure 4. Sediment basement interface (SBI) temperature as a function of crustal age. The predicted SBI temperature for sedimentation rates of 40 mMa^{-1} (PB04 at 3.5 Ma and PB06 at 5.7 Ma) and 25 mMa^{-1} (PB02 at 1.6 Ma, PB03 at 2.6 Ma and PB05 at 4.5 Ma) as obtained from Equation 2, are shown as the solid blue and dotted blue lines respectively. The black circles show the average SBI temperature (Table 1) based on the observed heat flow data for all five sites and the bars indicate their maximum and minimum range values. Observed SBI temperature at 6.9 Ma crust in ODP Hole 504B and Hole 896A (*Becker et. al.,* 1983; 2004) is shown as the red circle.
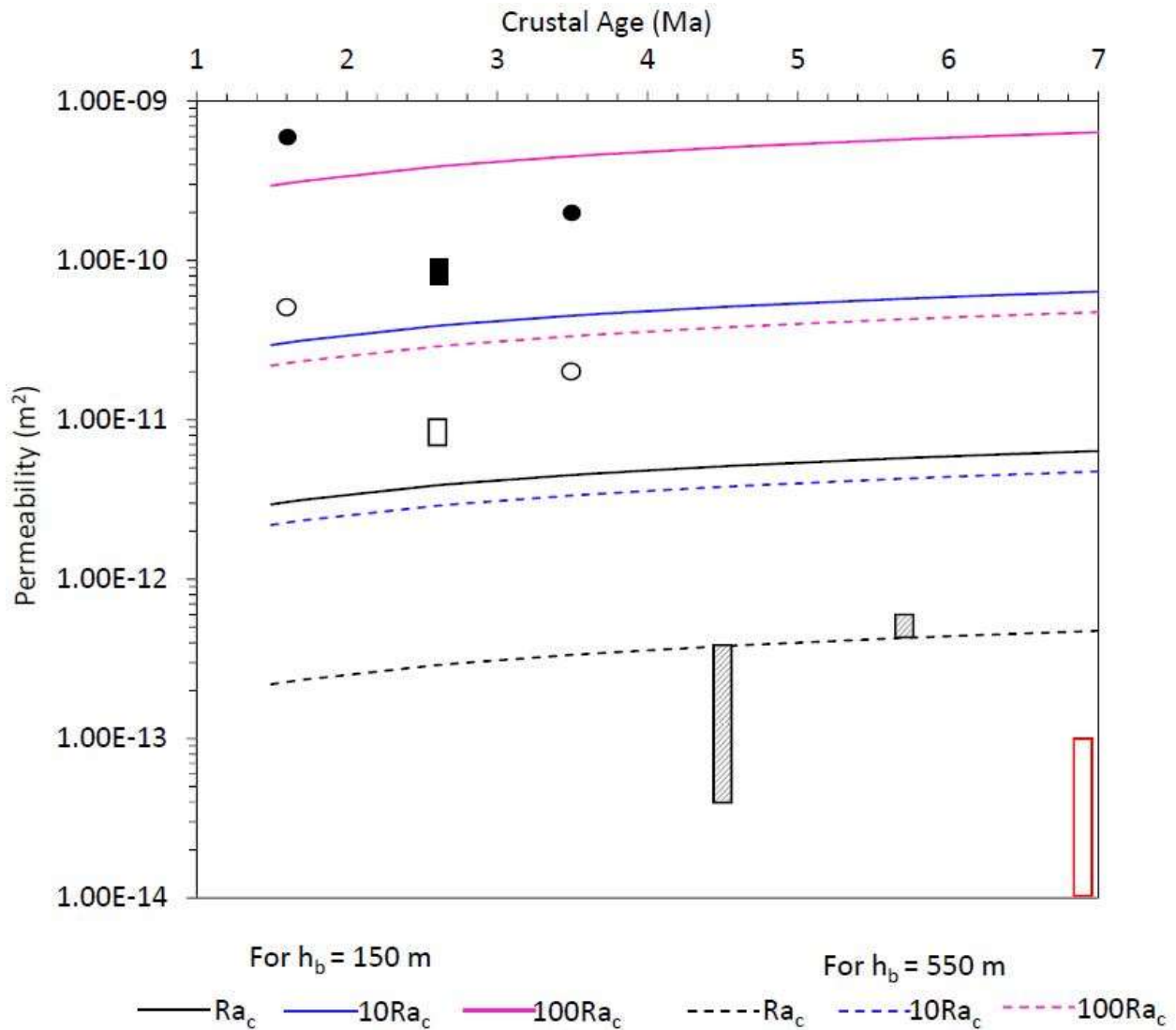
Figure 5. Estimated permeability of the crust as a function of crustal age for Ra_c, 10 Ra_c, 100Ra_c for h_b=150 m and 550 m. Solid black circles/rectangles are the estimated permeabilities/range of permeabilities at each site for h_b=150 m and open black circles/rectangles are for h_b=550 m. Hatched black rectangles are permeabilities where Rayleigh convection is at or near super-critical for h_b=550 m. Red open rectangle indicates the permeabilities at ODP Hole 504B in 6.9 Ma crust. The permeability values calculated are given to one significant figure and have a likely uncertainty of a factor of 2 for PB02 at 1.6 Ma, PB03 at 2.6 Ma and PB04 at 3.5 Ma but larger uncertainties for PB05 at 4.5 Ma and PB06 at 5.7 Ma.

Figure 6. Site PB02 (1.6 Ma) a) 19 heat flow measurements (black circles) as a function of distance from the CRR axis. Red crosses show sediment-basement interface (SBI) temperatures at each heat flow measurement. Grey boxes indicate heat flow sets A and B discussed in text. Blue dashed line shows best fitting exponential function (refer equation B.2) which is the solution to equation B.1. enabling the estimation of volumetric flow rate per unit length. R^2 shows the goodness of fit of the exponential equation. b) Pre-stack time migrated seismic image of PB02. The vertical axis is two-way travel time and horizontal axis is the distance from the CRR in km. Red box indicates possible discharge area. N=North and S=South. Note: faults are shown only where there is circumstantial evidence of enhanced heat flow which is interpreted as that caused by focused flow along a fault.

Figure 7. Site PB03 (2.6 Ma) a) 11 heat flow measurements (black circles) as a function of distance from the CR R axis. Red crosses show SBI temperatures at each heat flow measurement b) Pre-stack time migrated seismic image of PB03 plotted as in Figure 6. Yellow parallel lines indicate possible fault location and black arrow points at surface expression of possible fault. Red box indicates possible recharge area. N=North and S=South. Note: faults are shown only where there is circumstantial evidence of enhanced heat flow which is interpreted as that caused by focused flow along a fault.
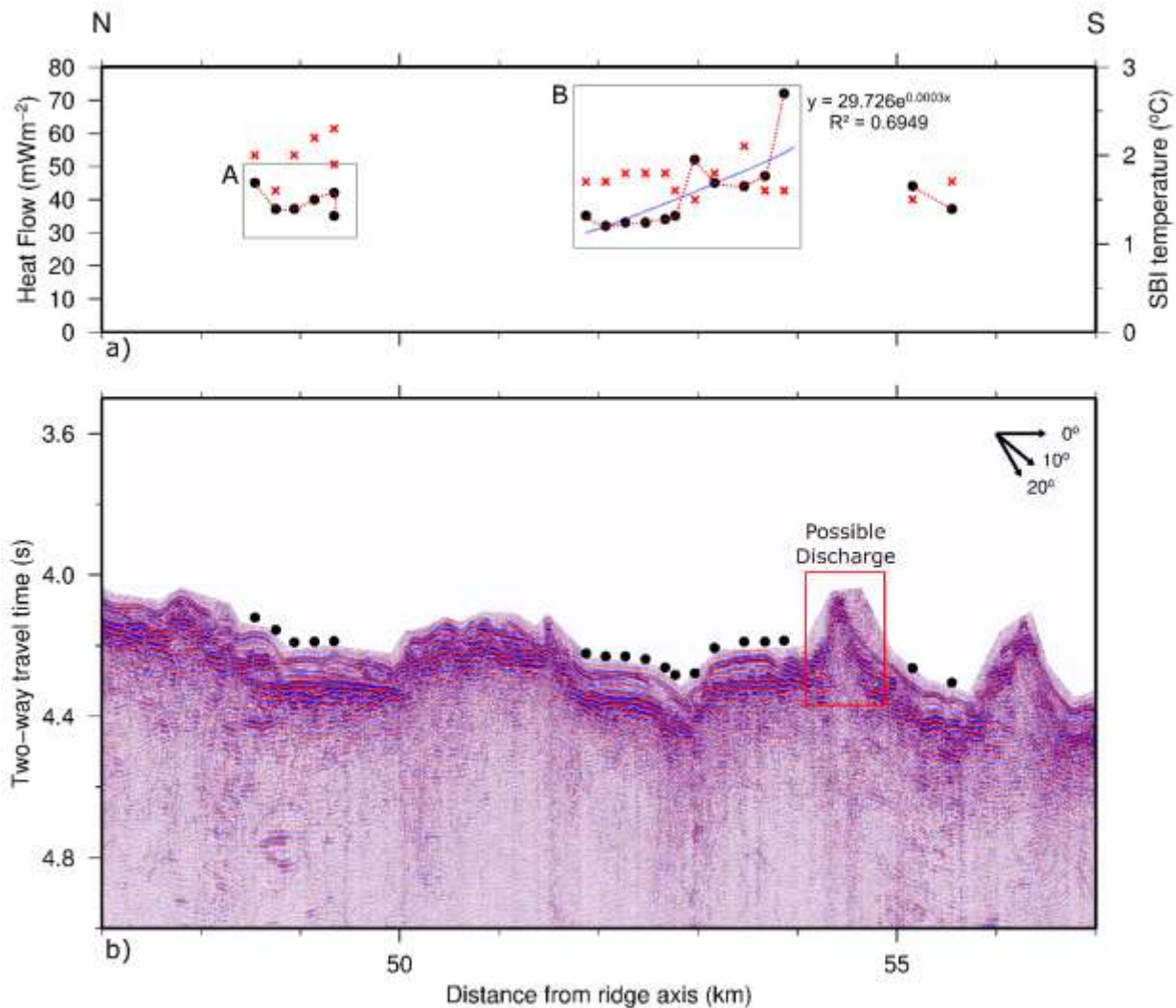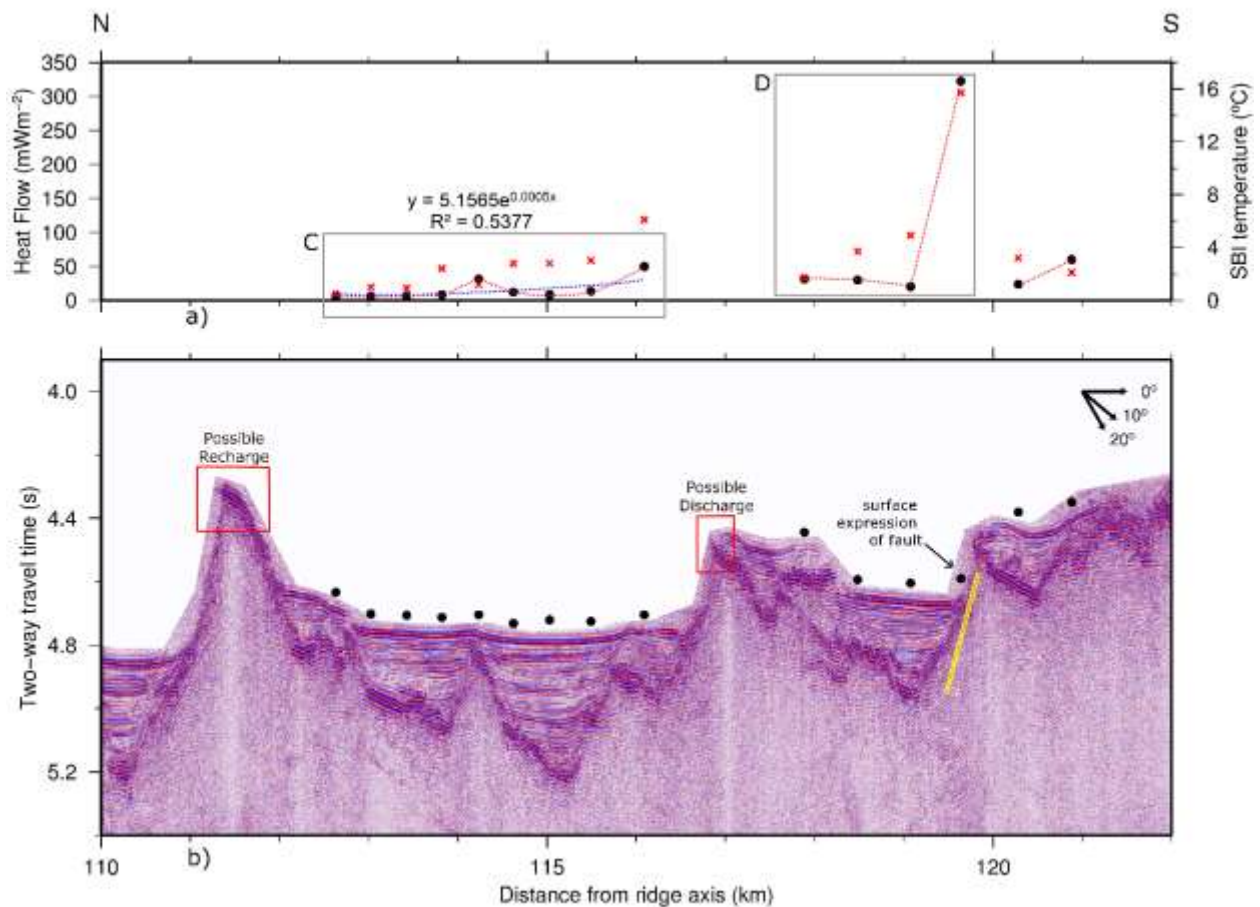
Figure 8. Site PB04 (3.5 Ma) a) 15 heat flow measurements (black circles) as a function of distance from the CRR axis. Red crosses show SBI temperatures at each heat flow measurement Grey boxes indicate sets C and D discussed in text. Blue dashed line shows best fitting exponential function (refer equation B.2) which is the solution to equation B.1. enabling the estimation of volumetric flow rate per unit length. R^2 shows the goodness of fit of the exponential equation. b) Pre-stack time migrated seismic image of PB04 plotted as in Figure 6. Yellow parallel lines indicate possible fault location and black arrow points at surface expression of possible fault. Red boxes indicates possible recharge and discharge areas. N=North and S=South. Note: faults are shown only where there is circumstantial evidence of enhanced heat flow which is interpreted as that caused by focused flow along a fault.
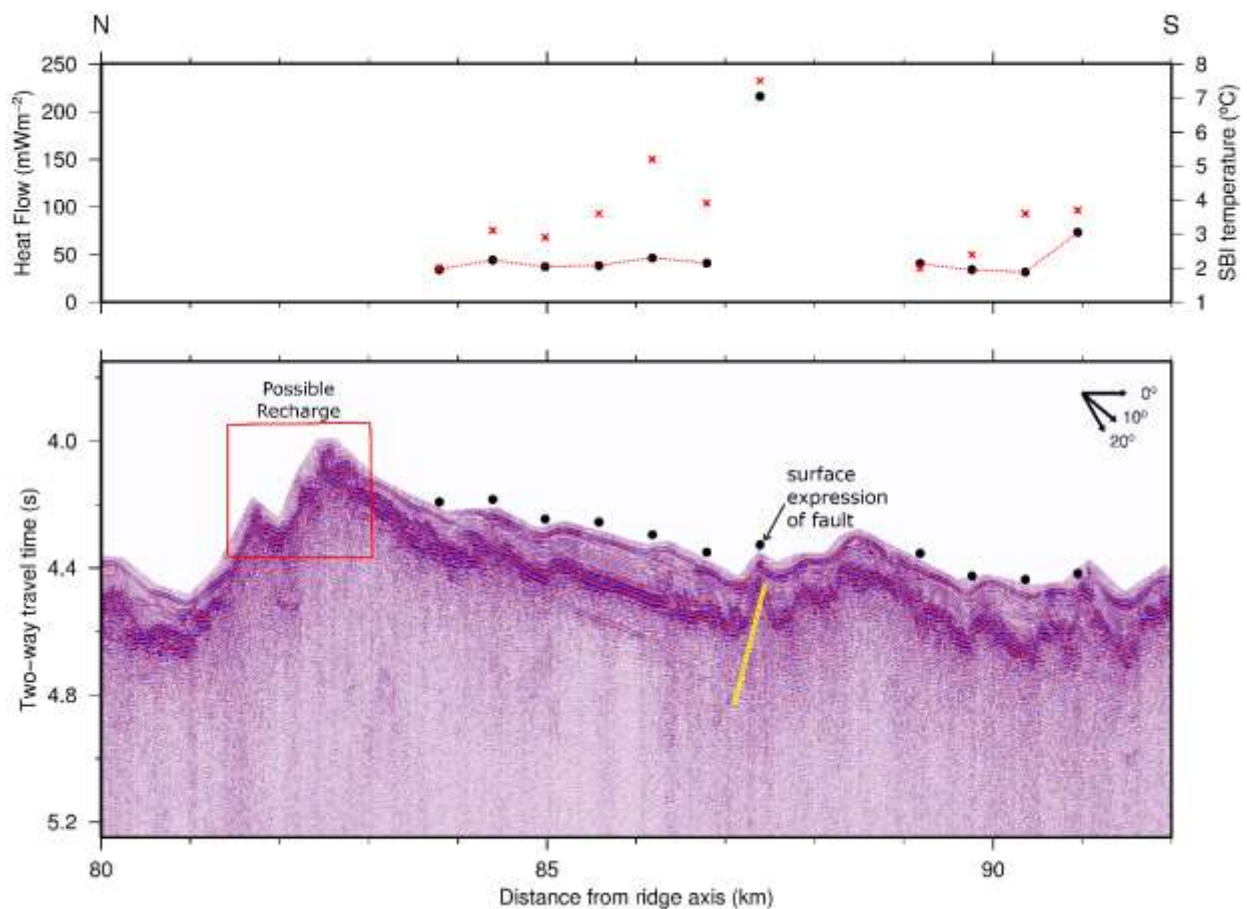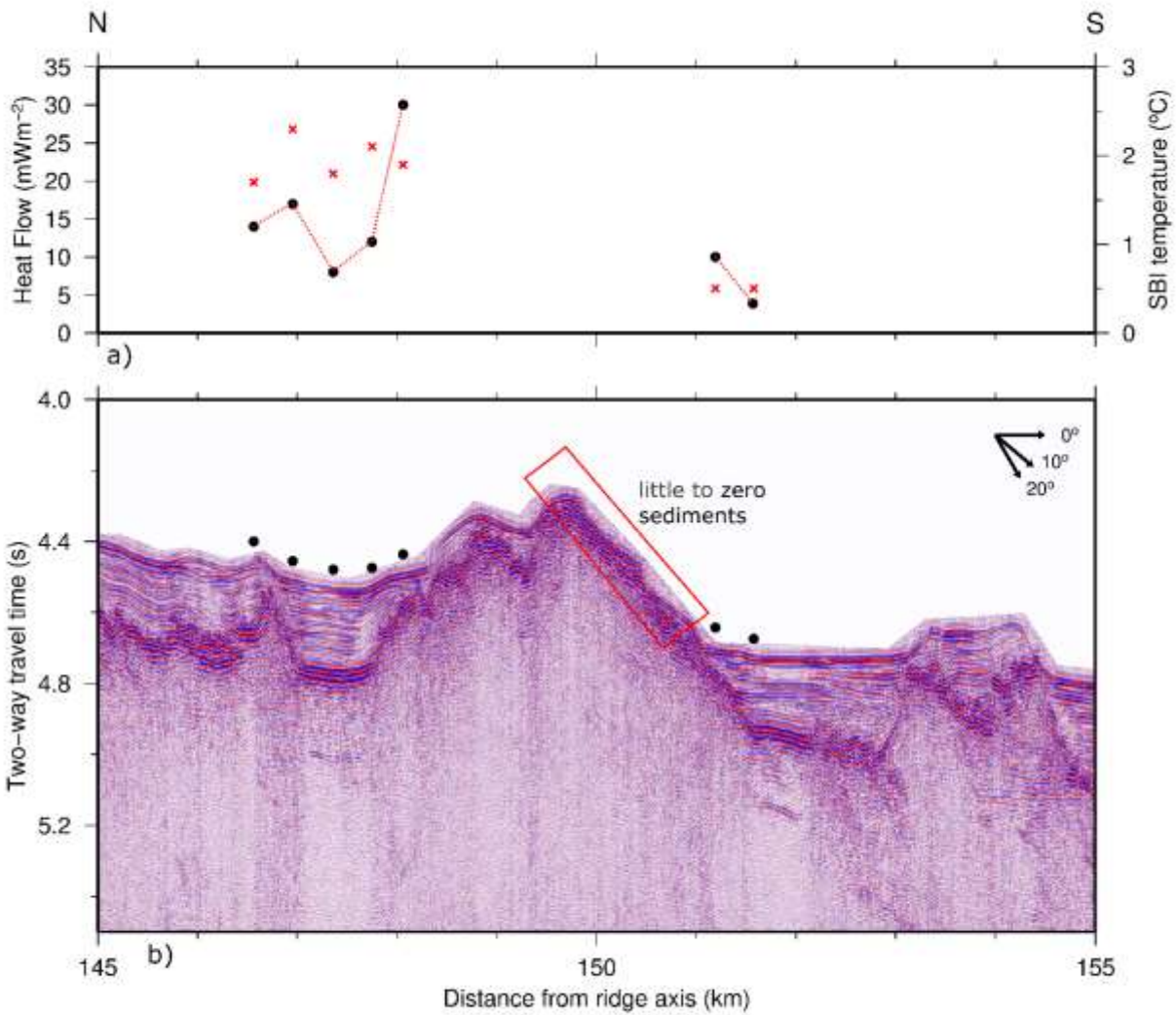
Figure 9. Site PB05 (4.5 Ma) a) 7 heat flow measurements (black circles) as a function of distance from the CRR axis. Red crosses show SBI temperatures at each heat flow measurement. b) Pre-stack time migrated seismic image of PB05 plotted as in Figure 6. Red box indicates area of little to no sediment. N=North and S=South. Note: faults are shown only where there is circumstantial evidence of enhanced heat flow which is interpreted as that caused by focused flow along a fault.
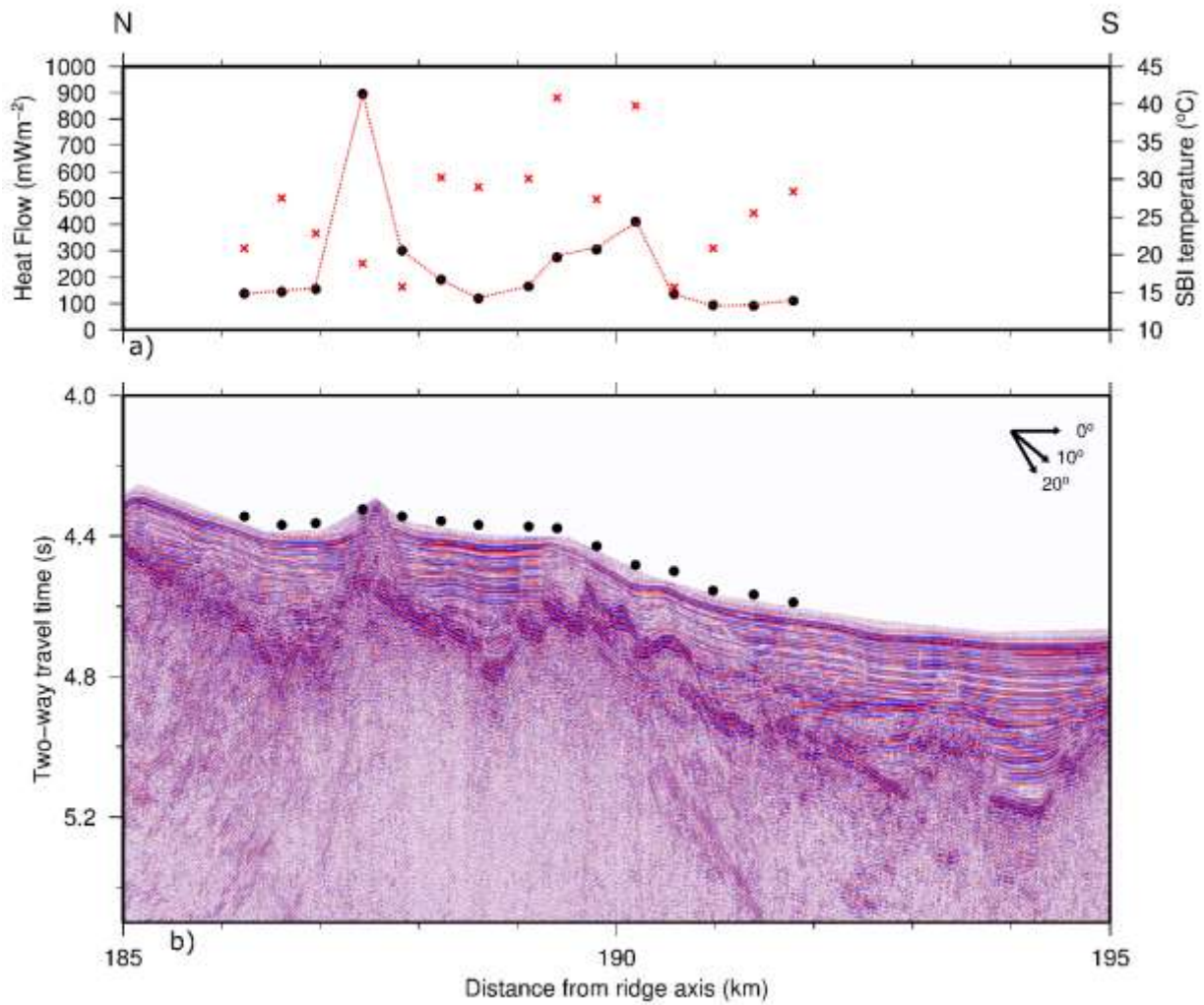
Figure 10. Site PB06 (5.7 Ma) a) 15 heat flow measurements (black circles) as a function of distance from the CRR axis. Red crosses show SBI temperatures at each heat flow measurement. b) Pre-stack time migrated seismic image of PB06 plotted as in Figure 6. N=North and S=South. Note: faults are shown only where there is circumstantial evidence of enhanced heat flow which is interpreted as that caused by focused flow along a fault.

Table 1. Conductive Heat Flow data from southern ridge flank of the Costa Rica Rift

Datum	Latitude	Longitude	Sediment Thickness	Thermal Gradient	Thermal Conductivity	Heat Flow	Sediment Basement Interface Temperature
	(°N)	(°W)	(m)	(°C km^{-1})	(W m^{-1} K^{-1})	(mWm^{-2})	(°C)
PB02 Age = 1.6 Ma							
PB02-01	2.8897	-83.6991	41	62	0.7	45	2.0
PB02-02	2.8878	-83.6992	40	51	0.7	37	1.6
PB02-03	2.8861	-83.6993	49	52	0.7	37	2.0
PB02-04	2.8843	-83.6993	50	55	0.7	40	2.2
PB02-05	2.8825	-83.6993	50	59	0.7	42	2.3
PB02-06	2.8825	-83.6994	50	48	0.7	35	1.9
PB02-07	2.8596	-83.6998	45	48	0.7	35	1.7
PB02-08	2.8578	-83.6999	49	45	0.7	32	1.7
PB02-09	2.8560	-83.6999	51	45	0.7	33	1.8
PB02-10	2.8542	-83.6999	49	46	0.7	33	1.8
PB02-11	2.8524	-83.7000	49	47	0.7	34	1.8
PB02-12	2.8515	-83.7001	42	48	0.7	35	1.6
PB02-13	2.8497	-83.7001	27	73	0.7	52	1.5
PB02-14	2.8479	-83.7002	36	62	0.7	45	1.8
PB02-15	2.8452	-83.7003	44	60	0.7	44	2.1
PB02-16	2.8433	-83.7003	31	65	0.7	47	1.6
PB02-17	2.8416	-83.7004	21	97	0.7	72	1.6
PB02-18	2.8299	-83.7008	30	61	0.7	44	1.5

PB02-19	2.8263	-83.7008	42	52	0.7	37	1.7
		Mean	42			41	1.8
PB03 Age = 2.6 Ma							
PB03-01	2.5711	-83.7074	57	46	0.7	33	2.0
PB03-02	2.5657	-83.7075	66	61	0.7	44	3.1
PB03-03	2.5604	-83.7076	72	53	0.7	37	2.9
PB03-04	2.5549	-83.7078	86	53	0.7	38	3.6
PB03-05	2.5495	-83.7079	104	65	0.7	46	5.2
PB03-06	2.5440	-83.7080	87	58	0.7	41	3.9
PB03-07	2.5386	-83.7083	32	278	0.8	217	7.5
PB03-08	2.5224	-83.7087	46	55	0.7	40	2.0
PB03-09	2.5171	-83.7089	66	48	0.7	34	2.4
PB03-10	2.5117	-83.7090	108	44	0.7	31	3.6
PB03-11	2.5064	-83.7091	47	103	0.7	73	3.7
		Mean	70			58	3.6
PB04 Age = 3.5 Ma							
PB04-01	2.3105	-83.7124	93	9	0.7	5	0.5
PB04-02	2.3069	-83.7125	135	9	0.7	7	1.0
PB04-03	2.3033	-83.7126	159	8	0.8	5	0.9
PB04-04	2.2997	-83.7126	202	11	0.7	11	2.4
PB04-05	2.2960	-83.7126	34	44	0.7	31	1.2
PB04-06	2.2925	-83.7127	218	18	0.7	12	2.8
PB04-07	2.2888	-83.7127	318	12	0.7	8	2.8
PB04-08	2.2846	-83.7127	194	19	0.7	14	3.0
PB04-09	2.2792	-83.7126	113	71	0.7	50	6.1

PB04-10	2.2630	-83.7125	53	43	0.7	30	1.7
PB04-11	2.2576	-83.7124	110	44	0.7	31	3.7
PB04-12	2.2522	-83.7126	225	29	0.7	20	4.9
PB04-13	2.2471	-83.7126	45	437	0.7	322	15.7
PB04-14	2.2413	-83.7126	123	34	0.7	24	3.2
PB04-15	2.2359	-83.7126	33	83	0.7	60	2.1
		Mean	137			42	3.5
PB05 Age = 4.5 Ma							
PB05-01	2.0038	-83.7187	110	19	0.7	14	1.7
PB05-02	2.0003	-83.7188	126	23	0.7	17	2.3
PB05-03	1.9966	-83.7189	184	12	0.7	9	1.8
PB05-04	1.9931	-83.7191	163	17	0.7	12	2.1
PB05-05	1.9903	-83.7186	62	42	0.7	29	1.9
PB05-06	1.9620	-83.7194	45	14	0.7	10	0.5
PB05-07	1.9585	-83.7197	146	5	2.0	3	0.5
		Mean	119			13	1.5
PB06 Age = 5.7 Ma							
PB06-01	1.6453	-83.7409	140	188	0.7	137	20.8
PB06-02	1.6419	-83.7405	176	198	0.7	144	27.5
PB06-03	1.6388	-83.7404	135	210	0.7	155	22.8
PB06-04	1.6345	-83.7397	19	1157	0.8	899	18.8
PB06-05	1.6309	-83.7393	48	397	0.8	301	15.7
PB06-06	1.6273	-83.7391	146	259	0.7	190	30.2
PB06-07	1.6239	-83.7388	226	161	0.7	118	29.0
PB06-08	1.6193	-83.7388	168	229	0.7	165	30.1

PB06-09	1.6167	-83.7387	136	382	0.7	276	40.8
PB06-10	1.6131	-83.7381	82	418	0.7	305	27.3
PB06-11	1.6095	-83.7377	89	570	0.7	412	39.8
PB06-12	1.6060	-83.7373	104	190	0.7	138	15.6
PB06-13	1.6024	-83.7368	203	130	0.7	94	20.8
PB06-14	1.5987	-83.7365	261	125	0.7	90	25.5
PB06-15	1.5951	-83.7361	235	156	0.7	111	28.4
		Mean	145			236	26.2
				Average	0.7	≈85	≈7

Table 2. Parameters and Values

Symbol	Definition	Value	Units
$a*$	Thermal diffusivity of fluid		$m^2\,s^{-1}$
c_f	Specific heat of water	4200	$J\,kg^{-1}\,K^{-1}$
g	Acceleration due to gravity	9.81	$m\,s^{-2}$
h_b	Basement thickness		m
h_s	Sediment thickness		m
k	Crustal permeability		m^2
k_{th}	Threshold crustal permeability		m^2
L	Horizontal fluid flow path length		m
q_{adv}	Advective heat flow		mWm^{-2}
q_b	Basal heat flux		mWm^{-2}
q_d	Heat flow at the discharge		mWm^{-2}
q_{obs}	Observed/Measured heat flow		mWm^{-2}
Ra	Rayleigh number		
Ra_c	Critical Rayleigh number		
T_b	Basement temperature		°C
T_d	Discharge temperature		°C
T_s	Temperature of the sediment layer		°C
T_{SBI}	Predicted temperature at the sediment-basement interface		°C
T_{SBI}^{obs}	Observed temperature at the sediment-basement interface		°C
T_{sp}	Spring temperature; Temperature of the upwelling fluids from a fault		°C
T_{sw}	Seawater temperature	0	°C

u	Darcian velocity of fluid		m yr^{-1}
u_z	Vertical velocity of fluids		m yr^{-1}
v_s	Sedimentation rate		mMa^{-1}
α	Thermal expansion coefficient of water	10^{-4}	°C^{-1}
λ_b	Thermal conductivity of the basement	2	Wm^{-1}K^{-1}
λ_s	Average Thermal conductivity of the sediments	0.92	Wm^{-1}K^{-1}
ν	Kinematic viscosity of the fluid	10^{-6}	m^2 s^{-1}
ρ_f	Density of water	1000	kg m^{-3}
τ	Age of Oceanic crust		Ma

Table 3. Permeabilities of sites PB02 thru 06 and ODP Hole 504B

Site	Age	Fractional Heat Flow	Advective Heat Flux	$< \Delta T_{SBI}^{obs} >$	Permeability	
	(Ma)	(q_{obs}/q_b)	(mW m^{-2})	(°C)	(m^2)[1]	(m^2)[2]
PB02	1.6	0.10	360	2	6 x 10^{-10}	5 x 10^{-11}
PB03	2.6	0.18	260	4	10^{-10} to 7 x 10^{-11}	10^{-11}to 7 x 10^{-12}
PB04	3.5	0.15	230	3	2 x 10^{-10}	2 x 10^{-11}
PB05	4.5	0.06	230	2	--	4 x 10^{-13}
PB06	5.7	1.00	0	26	--	5 x 10^{-13}
Hole 504B*	6.9	--	--	--	10^{-13} to 10^{-14} (Layer 2A)[3]	

[1]Assuming an aquifer thickness of 150 m.

[2]Assuming an aquifer thickness of 550 m.

[3](*Anderson & Zoback,* 1982; *Fisher et. al.,* 1990; Becker, 1996; Becker et. al., 2004)